Politecnico di Torino

Master's degree: Nanotechnologies for ICT's

A.a. 2021/2022

Graduation session: December 2022

Design of electrodes and processes for CO_2 valorization

Supervisors:

Prof. Fabrizio Pirri

Dott. Juqin Zeng

Dott. Adriano Sacco

Candidate:

Manlio Mignosa

Contents

Chapter 1

Introduction

1.1 Greenhouse effect and treatment methods for CO_2 mitigation

Earth's atmosphere prevents the heat, that comes from the Sun, from going back out from the atmosphere itself. This happens thanks to greenhouse gases present in the atmosphere, such as water vapour (H_2O), carbon dioxide (CO_2), methane (CH_4), nitrous oxide (N_2O), and ozone (O_3).

The Sun's energy is adsorbed by the surface of the earth, that riemits it as a longer wavelength infrared radiant heat, but due to greenhouse gases the atmosphere is opaque to infrared radiation. Greenhouse molecules, after absorbing, riemits this infrared radiation in all directions and warm the surrounding air and the other nearby greenhouse molecules (red arrow in Figure 1.1).
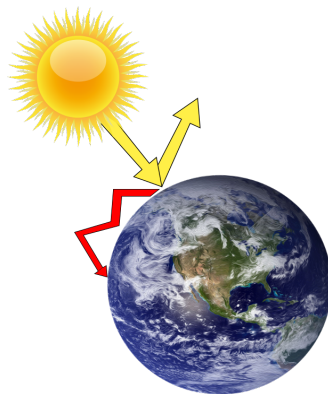

Figure 1.1: Greenhouse effect

With the natural effect of greenhouses gases, in our atmosphere, is possible to avoid that the temperature went down below the freezing point. Unfortunately nowadays the concentration of greenhouse gases is increasing and this causes the rising up of the temperature over the time [1].

For example, in the modern society the high consumption of fossil fuel is unavoidable to keep up the progress and this causes high CO_2 emission. The anthropogenic CO_2 emission influences negatively the climate change, the human health, food security and the sea-level rise [2].

Different mechanisms can be exploited to mitigate the concentration of CO_2 molecules in our atmosphere. These methods are shown in Figure 1.2

Treatment method	Characteristics	Drawback
Higher efficiency in electric energy production	• Use of innovative technologies usually • Efficiency improvements from 30% to 53% (IGCC)	High costs and long implementation times
Utilization of energy with better efficiency	• Requires a more conscientious attitude towards energy usage • Methods such as driving more fuel-efficient vehicles, using electrical appliances more efficiently	Difficult to plan and control in a unified manner
Fuel shift	• From coal to gas • Coal (950) > oil > gas (497)	Distribution of resources
Carbon capture and storage (CCS)	• Large potential in CO_2 storage • Storage in natural fields • Not accepted by many countries	Security and economic (costly, uncertainty, intensive energy requirements)
CO_2 conversion and utilization	• Recycles carbon • Reduces the extraction of fossil-C • Avoids emission of CO_2	

Figure 1.2: Mitigation methods. From Azeem Mustafa et al. [3]

The conversion and utilization mechanism is the most promising, with CO_2 conversion technologies driven by renewable energy sources Figure 1.3 [4, 5].
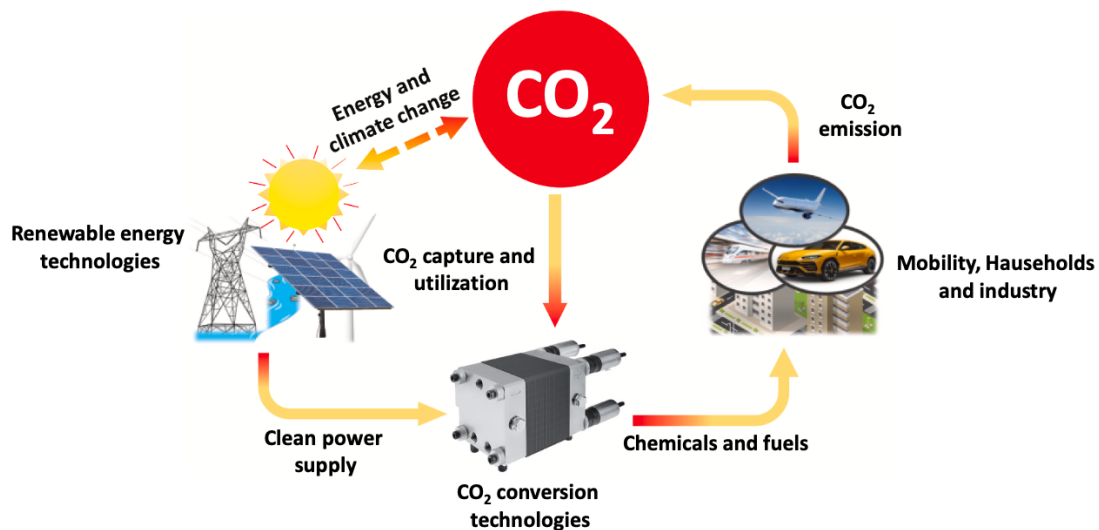

Figure 1.3: Anthropogenic carbon cycle. From Ashu Tufa et al. [4]

Organic molecules with high density of energy (as alcohols, CO and formate), can be obtained from CO_2 with conversion methods. The transmutation of carbon dioxide into fuels is economically and environmentally more advantageous, because the fuel trade is 10–13 times higher than the chemicals one [3].

1.2 Electrochemical CO_2 reduction

In Electrochemical CO_2 reduction (ERC) (using water, CO_2 and electricity (renewable energy)), it is possible to produce hydrocarbons [3].
ERC is now taking much more attention for large-scale deployment thanks to investments and researches on renewable energies. These efforts are lowering the electricity price and so ERC is becoming much more attractive [2].
Multi-carbons chemicals have much more potential, with respect to C_1 ones, in terms of socioeconomic value, market size, and energy density. Cu is the only known metal that can catalyse CO_2 in multi-carbons products with acceptable activity and efficiency [2, 6].

1.2.1 General aspects

CO_2 is a molecule with two double bonds (C=O, bond length=1.12Å, chemical bond energy=750 kJ mol^{-1}). It is chemically inert and can be activated only if high energy is provided [2].
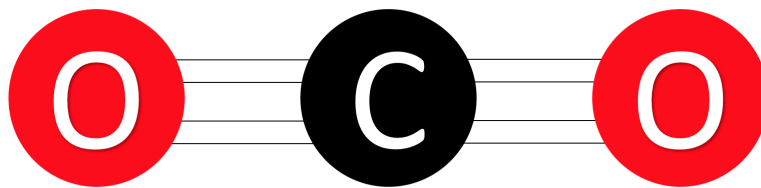
Figure 1.4: CO_2 molecule

The CO_2 reduction reaction (CO_2RR) occurs at the cathode of an electrocell system and the general formula is:

$$xCO_2 + nH^+ + ne^- = products + yH_2O \tag{1.1}$$
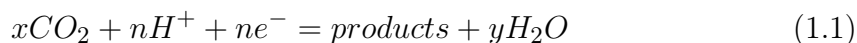
The steps that occur at the interface between the electrolyte and the electrode are shown in Figure 1.5 and the ECR for commonly reported chemicals are listed in Figure 1.6.
The development of an effective catalyst, that can be used to reach our needs about the CO_2 conversion in reusable products, can be achieved only after understanding the mechanisms involved in the formation of products. As shown in Figure 1.6 the potential for the Hydrogen Evolution Reaction (HER) process is paragonable to that one needed for other molecules production. For this reason HER is the

most competitive reaction that decreases the selectivity of the electro-reduction reaction. So several parameters should be taken into account, as: pH (that affects also the CO_2 solubility), temperature, potential, pressure, electrolyte, catalyst and optimized structure of the electro-cell [3].
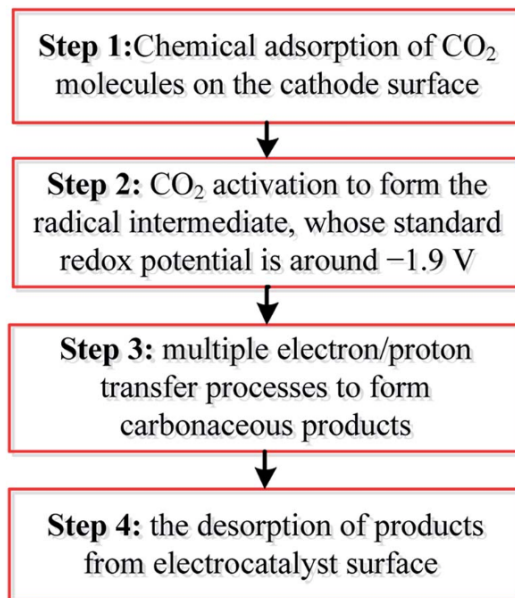

Figure 1.5: Steps for ERC reactions. Data from Azeem Mustafa et al. [3]

Products	Reaction	E^0/ V vs. RHE
O_2 (Oxygen)	$2H_2O = O_2 + 4H^+ + 4e^-$	1.23
H_2 (Hydrogen)	$2H^+ + 2e^- = H_{2(g)}$	0.00
	$CO_2 + 2H^+ + 2e^- = HCOOH_{(aq)}$	−0.12
	$CO_2 + 2H^+ + 2e^- = CO_{(g)} + H_2O$	−0.10
C_1 products (formic acid, carbon monoxide,	$CO_{2(g)} + 4H^+ + 2e^- = HCHO_{(aq)} + H_2O_{(aq)}$	−0.07
formaldehyde, graphite, methanol, methane)	$CO_2 + 4H^+ + 4e^- = C_{(s)} + 2H_2O$	0.21
	$CO_2 + 6H^+ + 6e^- = CH_3OH_{(aq)} + H_2O$	0.03
	$CO_2 + 8H^+ + 8e^- = CH_{4(g)} + 2H_2O$	0.17
	$2CO_2 + 2H^+ + 2e^- = C_2H_2O_{4(s)}$	−0.47
	$2CO_2 + 8H^+ + 8e^- = CH_3COOH_{(aq)} + 2H_2O$	0.11
C_2 products (Oxalic acid, acetic acid, acetaldehyde,	$2CO_2 + 10H^+ + 10e^- = CH_3CHO_{(aq)} + 3H_2O$	0.06
ethanol, ethylene, ethane)	$2CO_2 + 12H^+ + 12e^- = C_2H_5OH_{(aq)} + 3H_2O$	0.09
	$2CO_2 + 12H^+ + 12e^- = C_2H_4 + 4H_2O$	0.08
	$2CO_2 + 14H^+ + 14e^- = C_2H_{6(g)} + 4H_2O$	0.14
C_3 products (Propionaldehyde and propanol)	$3CO_2 + 16H^+ + 16e^- = C_2H_5CHO_{(aq)} + 5H_2O$	0.09
	$3CO_2 + 18H^+ + 18e^- = C_3H_7OH_{(aq)} + 5H_2O$	0.10

Figure 1.6: Half-reactions and reduction potential of CO_2RR. Data from S. Jiao, X. Fu, L. Zhang et al. [2]

There are distinctive pathways that lead to the formation of a particular product and in this paths there are electrochemical and chemical steps [2]. The surface binding energy of ECR intermediates can influence the rate-limiting step and the selectivity of the products in the ECR process [7, 8]. Typically a large reduction potential (-1.9 vs SHE) is required for the formation of *CO_2^- radical with the first electron transfer, and this is also considered as the rate-determining step [4].

Moreover the following formation of CO is considered the initial step to obtain multi-carbons products and *COCHO is the key intermediate for the formation of C$_{2+}$ products. By the way the difficulty towards C$_{2+}$ molecules formation, in Cu-based electrocatalysts, is related to C-C coupling, which may involve: at low overpotential the dimerization of *CO to form *OCCO and at high overpotentials the hydrogenation of *CO into *CHO species [2].

Nowadays there are different challenges related to overpotential, ohmic losses in the cell, selectivity, product separation, and stability [9].

Chemistry of CO_2 in aqueous media

Carbon dioxide interacts with water, forming carbonic acid [10]:

$$CO_2 + H_2O \leftrightarrow H_2CO_3 \tag{1.2}$$

At this point, CO_2 speciation towards bicarbonate (HCO_3^-) and carbonate (CO_3^{-2}) occurs:

$$H_2CO_3 \leftrightarrow HCO_3^- + H^+ \tag{1.3}$$

$$HCO_3^- \leftrightarrow CO_3^{2-} + H^+ \tag{1.4}$$

Bicarbonate solution is used, with the advantage that dissolved bicarbonate acts as a CO_2 reservoir. Dissolved CO_2, HCO_3^- and CO_3^{2-} are the active species for the CO_2RR [4].

When KOH solutions are used, the dissolved carbon ($H_2CO_3^*$ = sum of dissolved CO_2 and H_2CO_3) reacts with OH^- anions contained in the solution [11]:

$$H_2CO_3^*(aq) + OH^- \leftrightarrow HCO_3^-(aq) + H_2O(l) \tag{1.5}$$
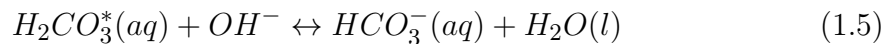
As shown in Figure 1.7, at alkaline conditions the presence of carbonate is higher [4]:

$$CO_2 + 2OH^- \leftrightarrow CO_3^{2-} + H_2O \tag{1.6}$$
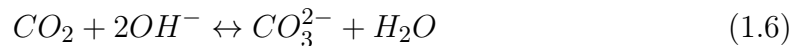
Anodic and Cathodic reactions

The reaction involved for the anodic part is the oxygen evolution reaction (**OER**, eq. (1.7) or (1.8)):

$$2H_2O \rightarrow O_2 + 4H^+ + 4e^- \, (Acidic Conditions) \tag{1.7}$$

$$4OH^- \rightarrow O_2 + 2H_2O + 4e^- \, (Alkaline Conditions) \tag{1.8}$$
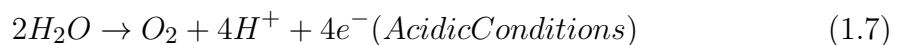
Figure 1.7: Bjerrum plot of carbonate speciation as a function of pH [12]
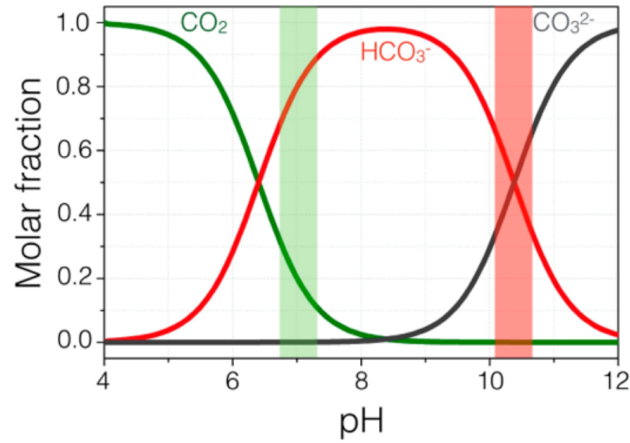
while the CO_2RR (eq. (1.9) or (1.10)) and the hydrogen evolution reaction (**HER, eq.** (1.11) **or** (1.12)) occur in the chatodic one:

$$CO_2 + nH^+ + me^- \rightarrow Products + H_2O (AcidicConditions) \qquad (1.9)$$

$$CO_2 + nH_2O + me^- \rightarrow Products + OH^- (AlkalineConditions) \qquad (1.10)$$

$$2H^+ + 2e^- \rightarrow H_2 (AcidicConditions) \qquad (1.11)$$

$$2H_2O + 2e^- \rightarrow H_2 + 2OH^- (AlkalineConditions) \qquad (1.12)$$
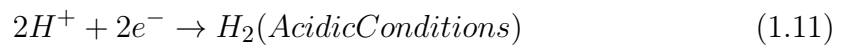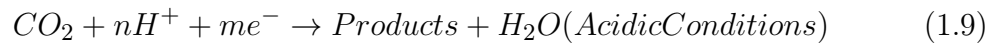
1.2.2   Electrocatalysis and parameters

CO_2 is a very stable molecule and it is not reactive. To convert carbon dioxide in other products it is necessary to supply energy to the system, decreasing the potential barrier needed for the reaction. For this reason we use electrical energy and we call this process electrocatalysis.
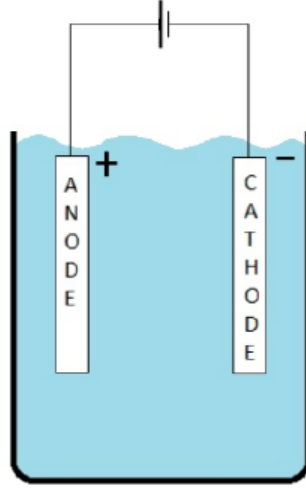

Figure 1.8: Electrocell

When we talk about energy potential we always have to say what is the reference that we choose. In electrocatalysis the reference is the standard hydrogen electrode (abbreviated SHE): this is a platinized platinum electrode and the redox reaction referred is the following one:

$$2H^+(aq) + 2e^- \rightarrow H_2(g) \tag{1.13}$$

SHE is defined at 0.000V potential in standard condition. To compare electrode in conditions different from the standard one, it is possible to use the reversible hydrogen electrode (RHE), using the Nerst equation:

$$E = 0.000 - 0.059 * pH \tag{1.14}$$

At this point, the energy potentials needed to start the CO_2 reduction reactions towards specific products ($E_{[vs.RHE]}$) are printout in scientific literature. So the energy formula for a specific CO_2RR becomes:

$$E_{[vs.RHE]} = 0.000 + 0.059 * pH + E^0_{[ref]} + E_{[vs.ref]} \tag{1.15}$$

Where $E^0_{[ref]}$ is the standard potential of the reference electrode versus SHE and $E_{[vs.ref]}$ is the potential applied at the electrode involved in the CO_2RR (Figure 1.9). Moreover to drive a sufficient reduction reaction it is necessary to take into account losses coming from different resistances [13]:

$$R_{tot} = R_{cathode} + R_{anode} + R_{ions} + R_{membrane} + R_{bubble,cathode} + R \qquad (1.16)$$

R_{tot} includes:

(1) The activation barriers for CO_2RR at cathode ($R_{cathode}$) and OER at the anode (R_{anode}).
(2) Ohmic losses from conduction of ions (R_{ions}) in the bulk electrolytes, ion transport across the membrane ($R_{membrane}$).
(3) Loss of active electrode area from the bubbles formation at the electrodes ($R_{bubble,cathode}$).
(4) The sum (R) of electrical resistances in other cell components and contact resistances between components.

So it is necessary to supply an overpotential to the system. So the formula becomes:

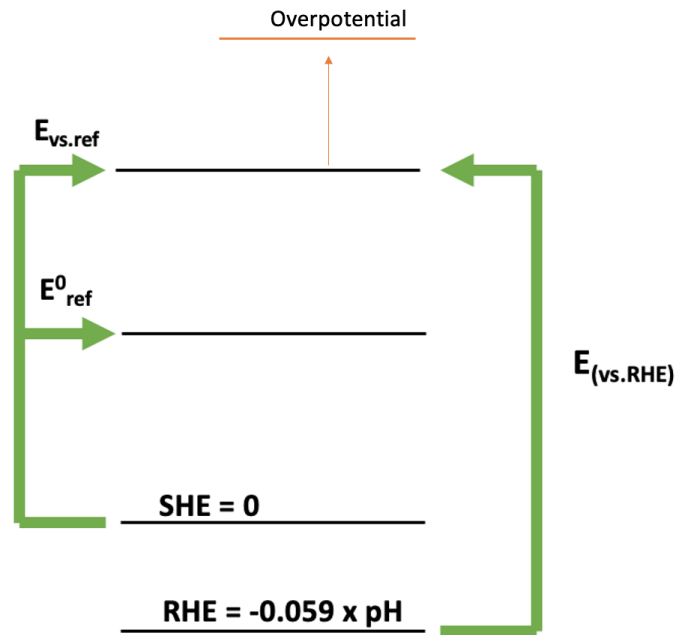$$E = E_{[vs.RHE]} + E_{overpotential} \qquad (1.17)$$

Figure 1.9: Energy levels

Current density

The current density is proportional to the reaction rate of the electroreduction process. So achieving high current value at low overpotential is a first goal:

$$J = I/A \tag{1.18}$$

where I is the total current (A) and A is the electrode area (cm^2).

Faraday efficiency (FE)

Faradaic efficiency is a parameter used to identify how much the electrode is selective for a certain product:

$$FE(\%) = \frac{nNF}{Q} * 100 \tag{1.19}$$

where n is the number of electrons involved in the reaction, N is the amount of generated products (mol), F is the faradaic constant (96485.33C/mol) and Q is the charge.

1.2.3   Electrolyzer

Current density, stability and faradaic efficiency are influenced by the electrochemical cell design. So in this section we will describe different cells design.

Batch Cell

The easy operation in ambient conditions makes the H-Type cell (Figure 1.10) a common configuration in academic research [2].
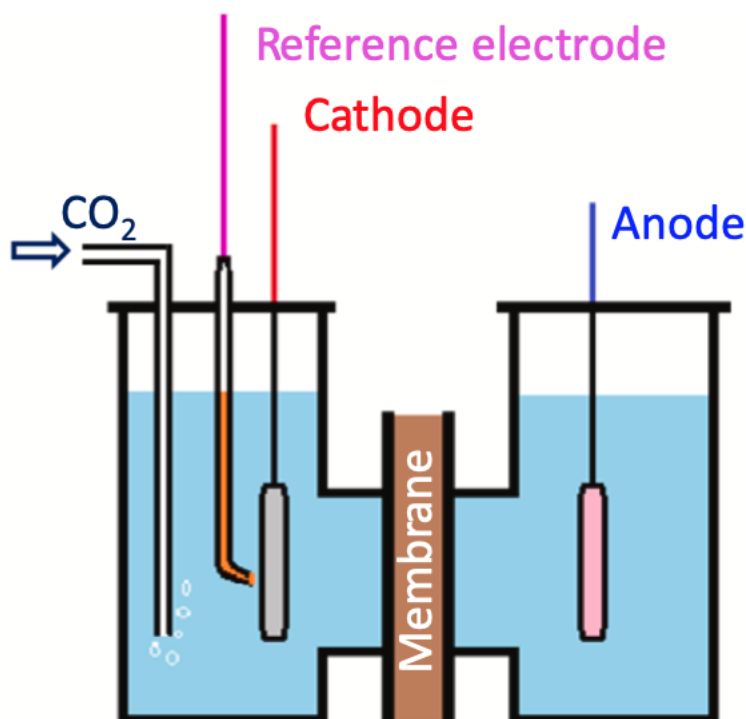

Figure 1.10: H-type cell. Image from Ashu Tufa et al. [4]

A lot of works were performed using an H-cell configuration [14, 15, 16]. The simplicity of this set-up makes it ideal to evaluate catalytic materials [17, 18, 19, 20]. In this cell the working electrode and the reference are in the cathodic part. In the anodic one there is a counter electrode. In the center a membrane, that allows the passage of some anions and cations, separates anode and cathode. At high over potential the mass-transport process becomes the rate-determining step and it rules the reaction: in fact at high potential there is a very fast conversion of reactants in products. However H-type electrolyzer production at large-scale is hampered by the low CO_2 solubility (33 mM at 25 °C, 1 atm in water) that limits the current under 100 mA cm^{-2}. Other drawbacks are the high ohmic loss, due to the long distance between the electrodes, and the limited electrode surface area [2].

Flow-cells

Flow-cells, in which there is a circulation of reactants and products, are a solution for the mass-transport limitation issue, that H-type cells have. Moreover they can be constructed in stacks guaranteeing higher current density ($\sim$1000 mA cm^{-2}). In particular, flow-cell with gas diffusion electrode (GDE) and membrane electrode assembly (MEA) has the flow-cell advantage (in which CO_2 is provided dissolved in a liquid phase [21] or in the gas phase [22, 23, 24]) and the reduced distance between anode and cathode, reducing the ohmic loss. These typologies are shown in Figure 1.11. A polymer electrolyte membrane (PEM), that allows the passage of some anions and cations, separates anode and cathode; avoiding the crossover of products.[2]

In **full-MEA** the electrolyte flows in both anode and cathode parts; in **exchange-MEA** the electrolyte flows just only in the cathode part, moreover the cathode is stacked with the membrane; the **aqueous GDE mode** is the same of the previous one with the difference that between cathode and membrane there is the electrolyte.[2]
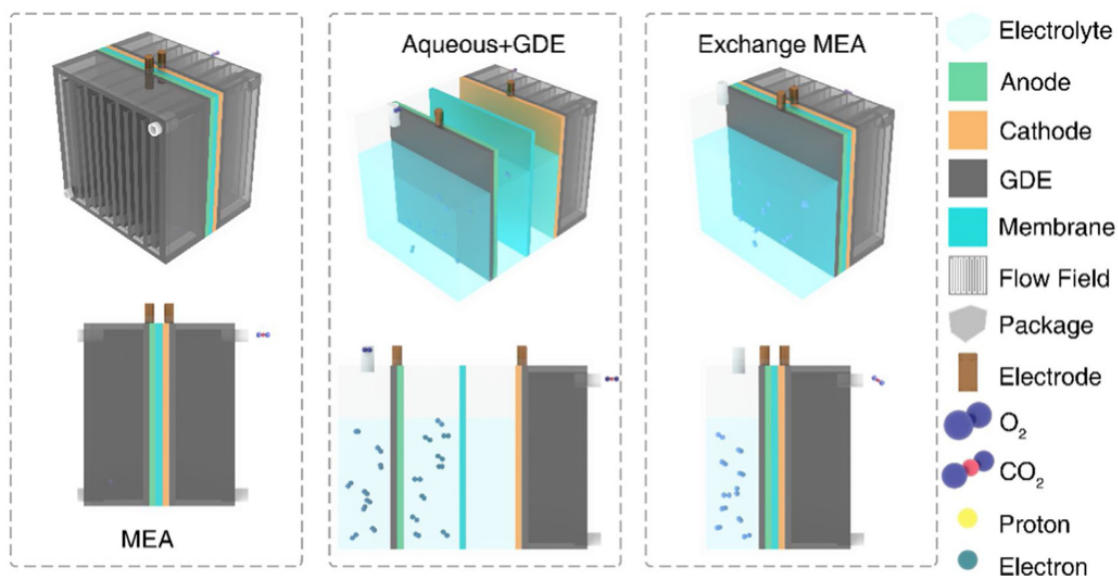

Figure 1.11: Emerging membrane electrolyzer. Image from S. Jiao, X. Fu, L. Zhang et al. [2]

Microfluidic electrolyzer

In a reactor with membrane, the pressure can be a problem [25]. In the microfluidic electrolyzer (Figure 1.12) there is a circulating liquid electrolyte that substitutes the membrane between anode and cathode [2]. So there is a thin spacer (<1mm) between anode and cathode, and the reference electrode is usually inserted in the flow stream [4]. This configuration was used by Kenis et al [26] to produce formic acid.

The performances of the microfluidic cell (MFC) can be influenced by channel length, GDE configuration, CO_2 concentration and flow rate [3].
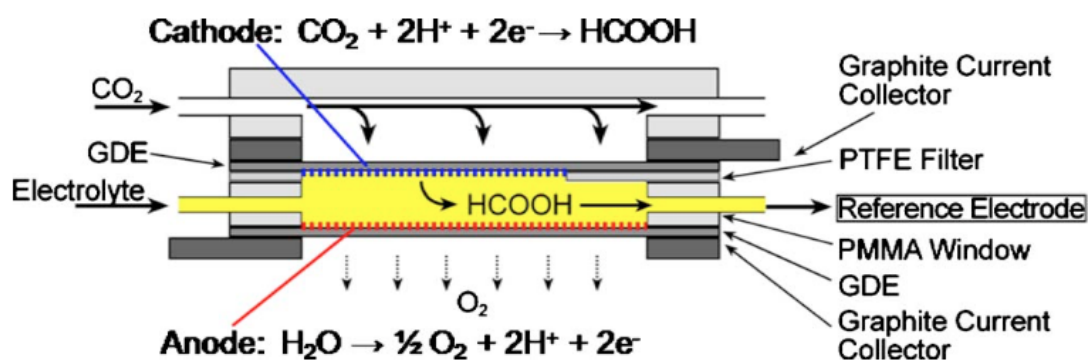

Figure 1.12: Microfluidic electrolizer. Image from Kenis et al. [26]

In an alkaline solution this type of reactor is more useful than the H-type one, because in alkaline solution carbon dioxide reacts to form neutral carbonate [3]. Using 10M KOH solution with a polymer-supported copper catalyst, current density of 473 mA cm^{-2} and faradic efficiency of 70% for ethane production was achieved [3].

Solid-oxide electrolysis cell (SOEC)

SOEC reactors can be used to produce syngas from CO_2 [27, 28, 29]. ERC, at high temperatures (800 K) can be realized in this type of reactor. Thanks to the high temperature environment the internal resistance can be decreased end the reaction kinetics can be increased. This lead to an increase of the efficiency. Moreover the solid electrolyte can be: a protonic conductor and a oxygen-ionic conductor. In protonic conductors water is transported to the anode and carbon dioxide is transported to the cathode. Protons produced at the anode are transferred to the cathode and react with CO_2 for low carbon molecules production. Using the other type of electrolyte a mix of water and CO_2 arrives at the cathode and it is transformed in CO and oxygen ions, that are transferred the anode and becomes oxygen gas. Mainly this type of reactor produces carbon monoxide and it has carbon and methane as by-products. This limitation is due to the high temperature used that causes the quick desorption of products from the surface of the electrode [3]. This type of cell

can lead to an increase of selectivity and efficiency, and the energy requirements are lower [27]. The drawbacks are related to the complicated chemistry and the degradation of electrodes and electrolytes at high temperature [30, 31, 32, 33, 34].

1.2.4 Membrane

The functions of the membrane are: to separate cathode from anode and to attenuate products crossover, but permitting the transfer of charge carriers. There are 3 types of membrane that can be used: **cation exchange membrane (CEM)** [35, 36, 37, 38], **anion exchange membrane (AEM)** [39, 40, 41, 42] and **bipolar membrane (BPM)** [43, 44].
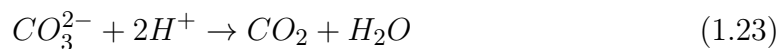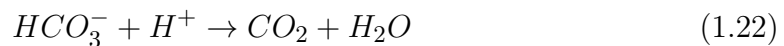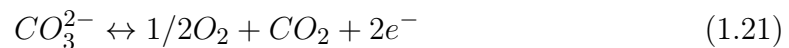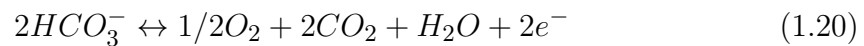
CEM

With CEM, cations can pass through the membrane, instead anions are retained. An example of this kind of membrane is Nafion (sulfonic acid groups with a polymer backbone), that showed high potential for C_{2+} products [2].
The migration of H^+ cations decreases the pH in the proximity of the cathode and this accelerates the HER process. For what concern the movement of metal cations from the anode to the cathode, this lead to an increase of the resistance and cell voltage. This gradient of metal cations can be compensated by formic acid and acetic acids, that form the corresponding metal salts [45].

AEM

With AEM, anions can pass through the membrane, instead cations are retained. The goal, with this type of membranes, is to circulate an alkaline solution at the anode side, promoting the membrane conductivity and the use of non noble catalysts for OER (eq. 1.20 - 1.21) [4].
AEM is very compatible for ERC, because the majority of charge carriers are carbonate and bicarbonate anions. When ions are transported towards the anode, they are consumed:

$$2HCO_3^- \leftrightarrow 1/2O_2 + 2CO_2 + H_2O + 2e^- \tag{1.20}$$

$$CO_3^{2-} \leftrightarrow 1/2O_2 + CO_2 + 2e^- \tag{1.21}$$

$$HCO_3^- + H^+ \rightarrow CO_2 + H_2O \tag{1.22}$$

$$CO_3^{2-} + 2H^+ \rightarrow CO_2 + H_2O \tag{1.23}$$

The formation of CO_2 at the anode side is called pumping effect, and it is proportional to the current density [4].

Membrane-based flow-cells, that utilize AEM membrane, show the best performance, especially for C_{2+} molecules production [2]. Using AEM there are less polarization losses and higher current densities compared with CEM [3].

With AEM there is also a CO_2 pumping phenomena that can occurs and the quantity of CO_2 crossover can be higher than the reduced one [4].

BPM

BPM (Figure 1.13) is composed by an AEM and an CEM in contact, creating also an interfacial layer in between. And they can operate in forward bias and in reverse bias [4]:
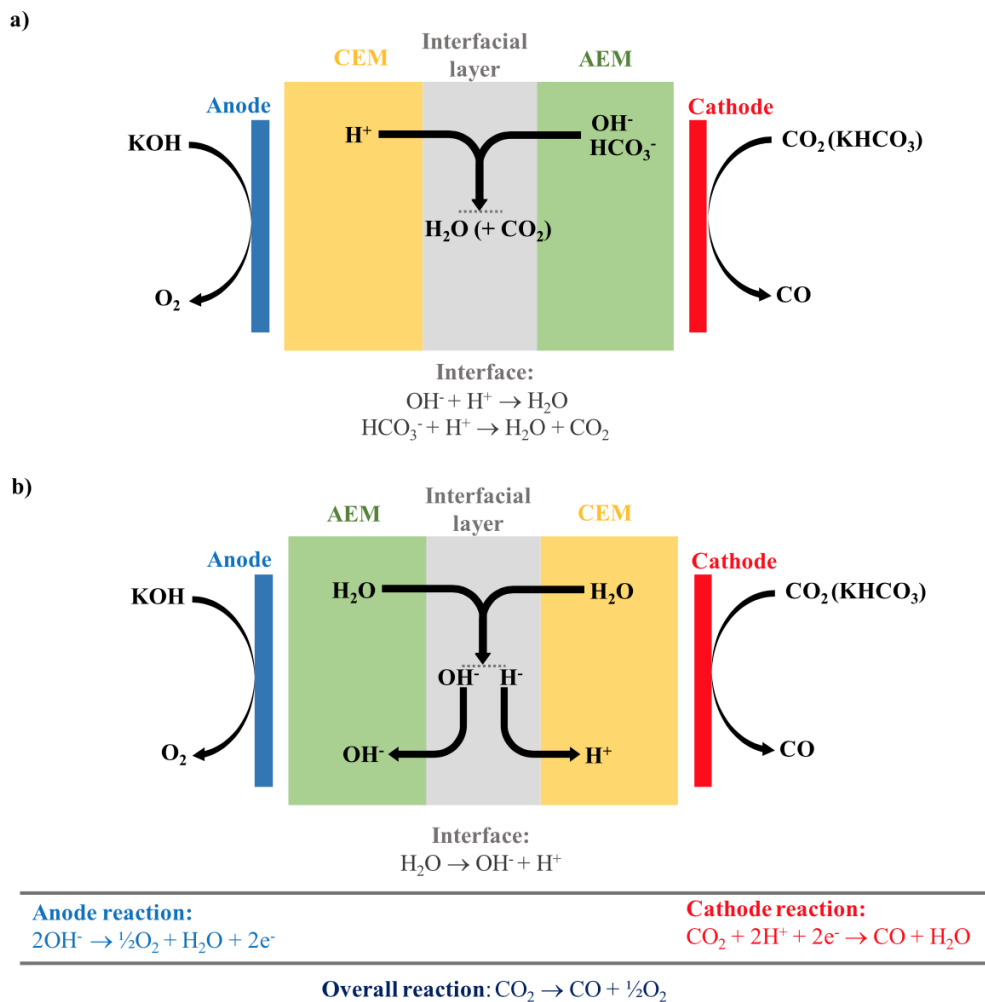

Figure 1.13: Configurations of BPM-based CO_2 electrolyzer. a) Forward bias b) Reverse bias

In forward bias H_2O and CO_2 are produced at the interfacial layer; instead water dissociation occurs in reverse bias mode [4].

This type of membrane has the advantage to maintain the same level of ph, leading the migration of H$^+$ and OH$^-$ ions.; this allows to use inexpensive anode and cathode electrocatalysts. The disadvantage seems to lie on the high voltage drop across the membrane that causes a lower energy efficiency [2].

1.2.5   Electrocatalysts design

It is possible to classify metallic electrode according different classification techniques. Most of these ones are related to the type of product produced.
Hori et al [46] found 4 groups: (1) Pb, In, Sn and Bi produce formate in aqueous solution; (2) Au, Ag and Zn produce CO; (3) Cu produces hydrocarbons and alcohols; (4) Pt, Ni, Fe, and Ti favour H_2 formation.
Also surface morphology influences the performance of CO_2R. For example, to increase the low-coordination sites (more active for carbon dioxide reduction) nanostructured metal surface should be used [4].
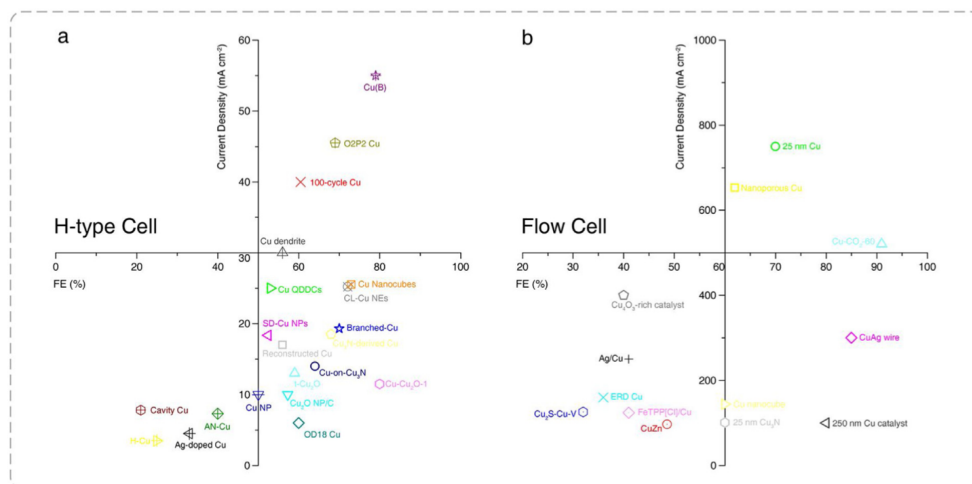

Figure 1.14: Current state-of-the-art electrocatalyst converting CO_2 into the C$_{2+}$ products in the (a) H-type cell configuration and (b) flow-cell setup. Image from S. Jiao, X. Fu, L. Zhang et al. [2]

The electrochemical conversion of carbon dioxide in hydrocarbons and oxygenates has obtained big attention due to the high energy density and the utilization as fuels. Cu till now is the only one that can be used to produce these types of products [4]. In Figure 1.14, FE and Current density, for different electrocatalysts, are shown. Cu with 25nm of particle diameter is the actual best performer for C_{2+} products.

When we talk about electrocatalysts design we should always take into account the range-scale that we are taking into account because tuning the different physical-chemical characteristics (referred at the different scales) change the chemistry of the products [2]:

Atomic-scale

At this scale we refer on: vacancy, single-atom catalyst, adatom and chemisorbed molecules [2].

Nanoscale

At this scale we refer on: facet, subsurface oxygen, grain boundary, alloying and intermetallic [2]. The (111) facet favors the production of C_1 products; instead the (100) and (110) ones favor the production of C_2 chemicals [47, 4]. This is attributed to the stabilization of different intermediates for each facet orientation: -CHO intermediate ((111) facet) for CH_4 and C_2H_4; CO dimer ((100) facet) for C_2H_4 [48].

Mesoscale

At this scale we refer on: morphology, porosity, roughness, particle size, interface. [2] It seems that decreasing Cu particle size leads to an increase of the selectivity for CO and H_2 [4].

The kinetics of planar or porous catalytic layer depend on the rate of CO_2 transfer to and from the electrolyte. To address this limitation it is possible to use a GDE Figure 1.15.
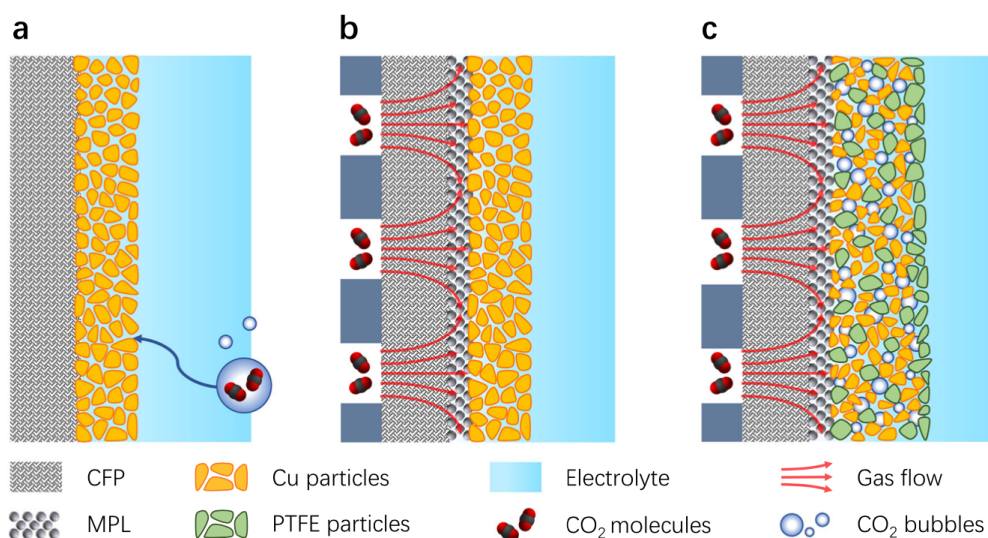

Figure 1.15: Schematics of: (a) normal electrode (b,c) gas diffusion electrode [5]

The type and nature of GDE influence the mass transfer and the kinetics of the reduction process[4]. In any case the improved performances are attributed to the three phase interfaces (solid catalyst, liquid electrolyte and CO_2 gas), but this statement is still under debate[5]. To fed CO_2 gas directly from the backside of the

electrode it is necessary to use a hydrophobic component to prevent the flooding of the electrolyte in the gas chamber; so just a microporous layer (MPL) can be added to the carbon fiber paper (CFP) (in Figure 1.15b), or also polytetrafluoroethylene (PTFE) particles can be added to the catalyst layer to improve the hydrophobicity Figure 1.15c).

1.2.6 Electrolyte

The correct design of the electrolyte has an important impact on the ECR, it should have appropriate proton donating and buffer capacity. Also electrostatic interaction should be taken into account. So understanding how cations and anions change electrochemical reaction is significant, but also challenging [2].

Cation effect

Cations accumulate in the proximity of Cu electrodes and seem to stabilize polar or highly polarizable intermediates with electric field interaction. This field stabilization lead to a decreasing potential barrier for the *CO_2 adsorption and C-C coupling [2, 3]. Larger cations in polycristallyne Cu enhance the production of C_{2+} molecules and decrease the HER [3]. It seems that cations are not completely adsorbed to the surface of the electrode, but tend to accumulate in the vicinity of the electrode, changing the spread of intermediates, binding energy and blocking active sites. Moreover, a short amount of cations is needed in some cases to obtain specific chemical products [3]

Anion effect

Bicarbonate anions (HCO_3^-) can stabilize the decreasing of pH thanks to the equilibrium with water [2] (Equation 1.24)

$$HCO_3^- + OH^- \leftrightarrow CO_3^{2-} + H_2O \tag{1.24}$$
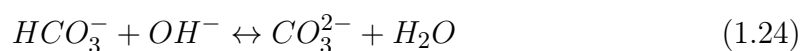
HCO_3^- can also favour the transportation of carbon dioxide from the bulk region towards the catalyst surface [2].
The changing of local pH influences the CO_2 electrocatalysis [2, 3] but it is also suggested that it cannot sufficiently impact the selectivity; so probably is the potential of buffering anions to generate hydrogen molecule, close to the surface of the electrode, that can influence the selectivity [3]. Adsorption of halides anions stabilizes intermediates with partial charge donation from the halide anions to CO_2. In Cu-based electrochemistry halide ions can suppress HER, changing the morphology and structure of the copper surface.[3]
Anion can also tune the coordination environment of adsorbed *CO [2] and facilitate the production of C_{2+} molecules [2, 3].

pH effect

C_{2+} chemicals production can be enhanced with an increasing of pH close to the active sites (local pH), thanks to the suppression of the competitive HER[2, 3]. Using electrolyte with high pH value is now a general methods to increase the selectivity towards multi-carbon products [2].

1.3 Aim of the project

Among the different products that can be produced by CO_2RR, C_{2+} molecules are preferable due to their intrinsic value as feedstock for industrial processes. Only Cu is the element able to produce this type of molecules [49]. For this reason Cu was used as electrode material for this project. The purpose of this work is to characterize Cu electrodes fabricated with different loadings to understand the products for which they are selective and what are the electrical parameters that maximize the amount of these products.

The loadings of the fabricated electrodes are: 0.125 $mg*cm^{-2}$; 0.25 $mg*cm^{-2}$; 0.50 $mg*cm^{-2}$; 1.0 $mg*cm^{-2}$; 2.0 $mg*cm^{-2}$; 3.0 $mg*cm^{-2}$. Moreover 2 different Cu powders with 2 different particles diameters were used: 25nm and 50nm.

Chapter 2

Materials and methods

2.1 Electrode fabrication

Fabrication of the electrodes was done by drop casting technique, which is widely used thanks to its simplicity. With this method a liquid suspension, that contains particles of the material of interest, is deposited on the surface of a substrate drop by drop (Figure 2.1)
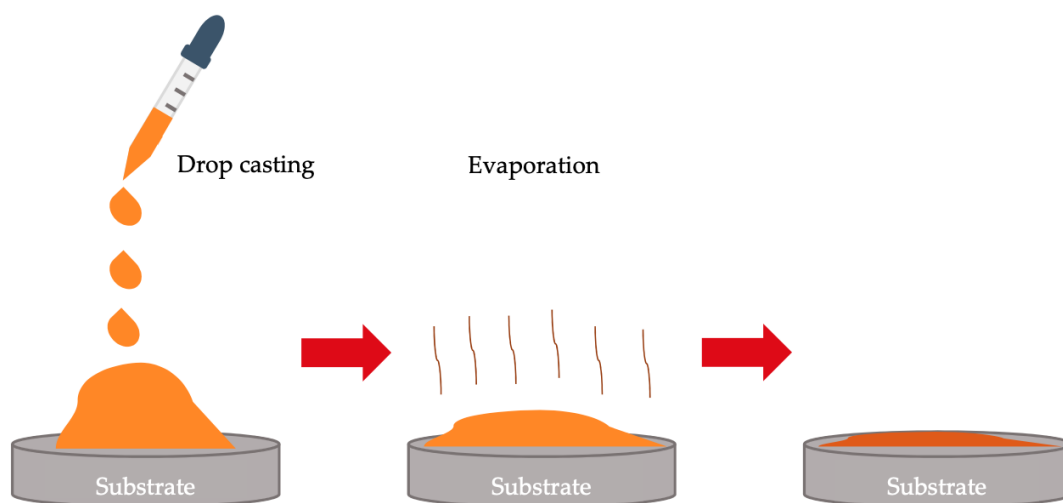

Figure 2.1: Drop casting method. Figure from Edward Bormashenko et al [50]

For this project GDL composed of carbon paper with a Microporous Layer (MPL) that has been PTFE treated to 5 wt% was used as main substrate material (baseline composition), but also other substrate compositions were used. An example of result is shown in Figure 2.2.

The drop casted suspension is a mixture of Cu nanoparticles, Nafion and Iso-propanol. After the evaporation of the solution the electrode was positioned on the cathode base with a copper tape to ensure the electrical connection with the base, and with a teflon tape to delimitate the electrode area of interest (Figure 2.3):
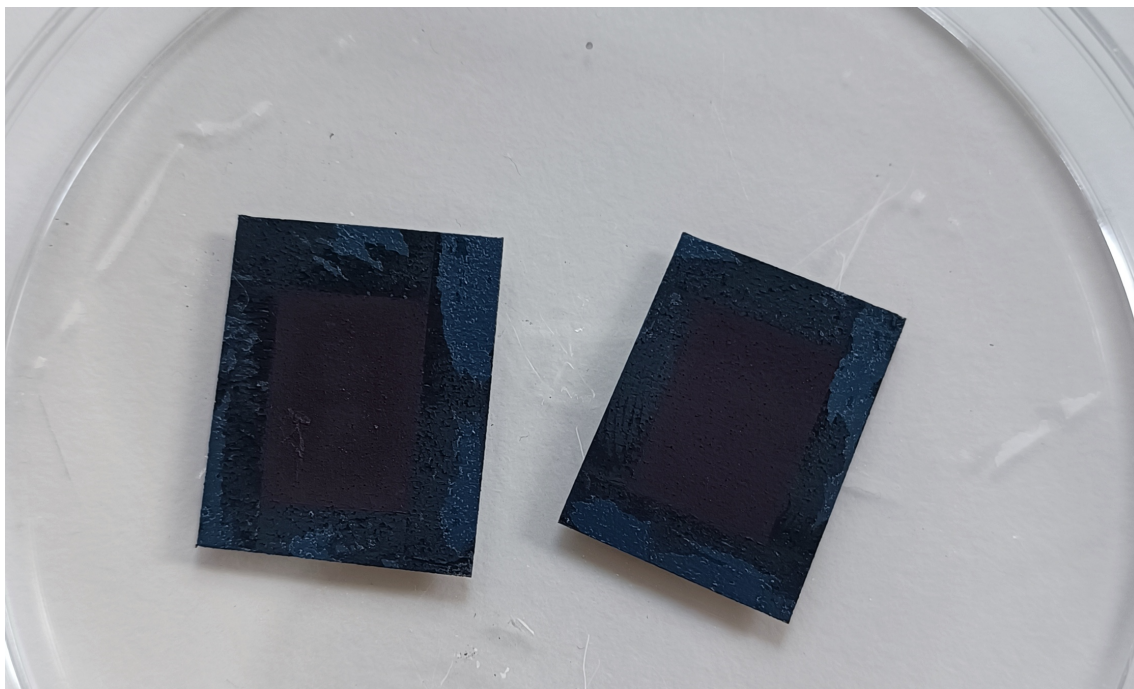
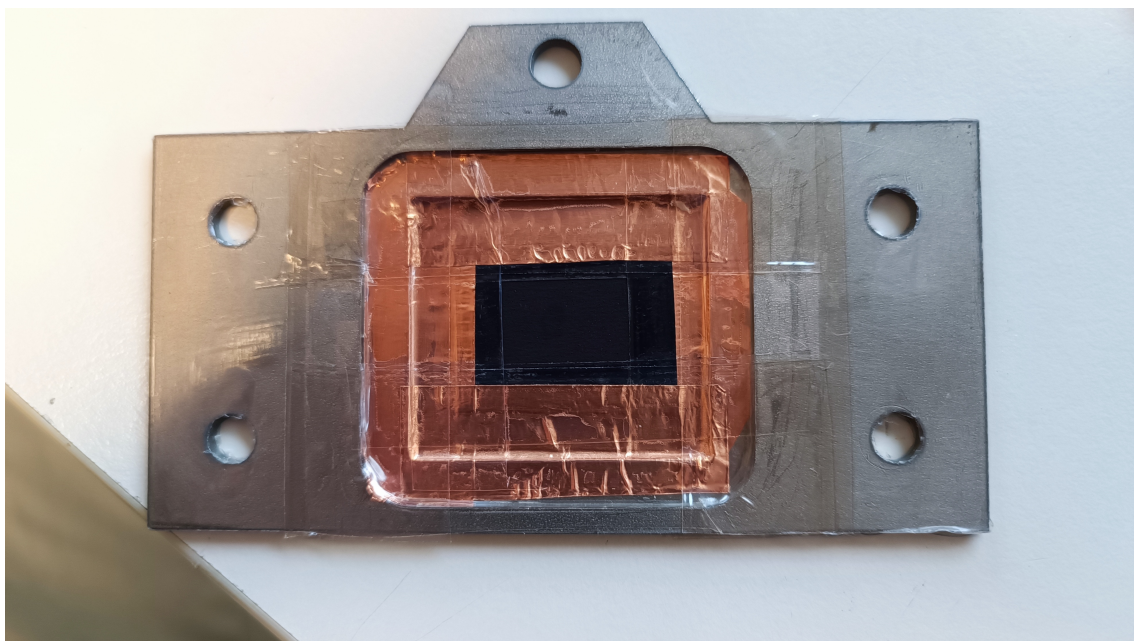Figure 2.2: Electrode modified by a drop casted suspension

Figure 2.3: Electrode on the cathode base

2.2 Electrode characterization

The characterization of electrodes was done by the following methods:
1) Chronopotentiometry (CP) was used to study the CO_2 reduction reaction at constant current densities.

2) High Performance Liquid Chromatography (HPLC) and Gas Chromatography were used to identify and to quantify the electrochemical products.

3) Cyclic Voltammetry (CV) and Electrochemical Impedance Spectroscopy (EIS) were performed to investigate the electrochemical properties of the electrodes.

4) X-Ray diffractometry (XRD) was used to examine the composition of the electrode material.

2.2.1 Chronopotentiometry

Chronopotentiometry (CP) is a method used in electrochemistry to study chemical reaction mechanisms and kinetics. In this method a constant current is imposed for a certain interval of time, and the potential of the working electrode is measured and recorded as function of time. When the experiment begins the redox-active species diffuse towards the working electrode to balance the electron current. This happens until the concentration of redox species (diffusion-limited) becomes zero at the surface of the electrode.

$$O + ne^- \rightleftarrows R \tag{2.1}$$

Cosidering the general equation (2.1), when O concentration becomes zero at the electrode surface, the potential of the electrode reaches more negative values with a transient time τ. Moreover the transient time has an analytic connection with the diffusion coefficient and concentration of the O species:

$$\tau^{3/2} = \frac{2C_0^* nFAD_0^{1/2}}{3\beta} \tag{2.2}$$

where C_0^* = concentration of O, n = electrons number, F=Faraday's Constant, A = working electrode area, D = diffusion coefficient, and β = sweep rate.

CP measurements were performed with a CH 700E Series Bipotentiostat at room temperature in a two-compartment three-electrode cell with KOH 1M as electrolyte Figure 2.4. An ion exchange membrane (Sustainion) is used to separate the compartments, sputtered IrO_2 was used as anode material (i.e. the counter eletrode) and Ag/AgCl as reference electrode (1mm, leak-free LF-1).

The scheme of reactor is shown in Figure 2.5: the CO_2 is supplied from the backside of the cathode that, in fact, is a gas diffusion electrode (GDE), and the electrolyte flows both in the anode and in the cathode parts.

The setup used is shown in Figure 2.6 and Figure 2.7: the liquid path is represented by light blue arrows, instead the gas path is represented by red arrows. It is possible to see that KOH electrolyte is recirculated just only in the anode. The reason is that KOH solution reacts with CO_2 forming potassium bicarbonate and this would change the chemistry of the electrolyte.
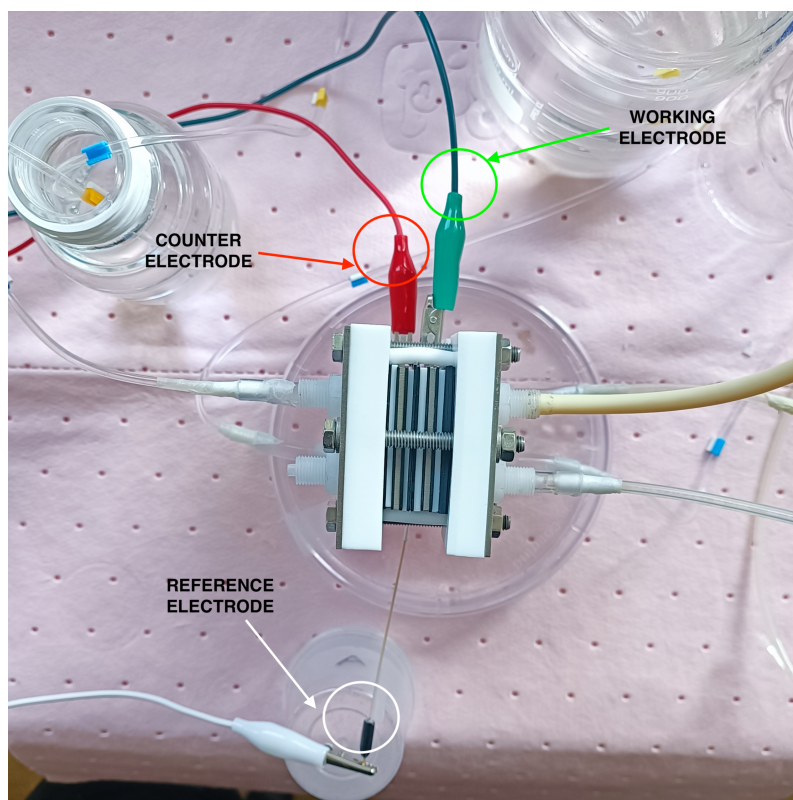
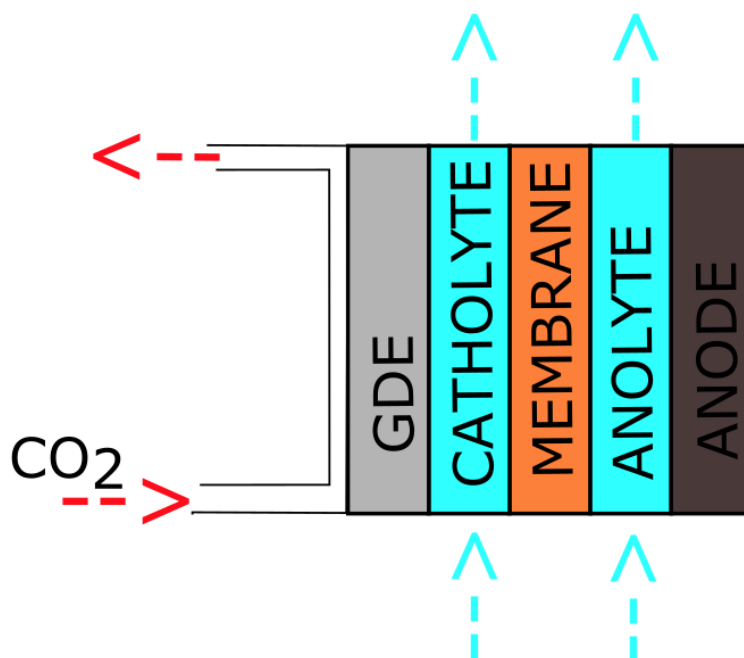Figure 2.4: Three-electrode cell
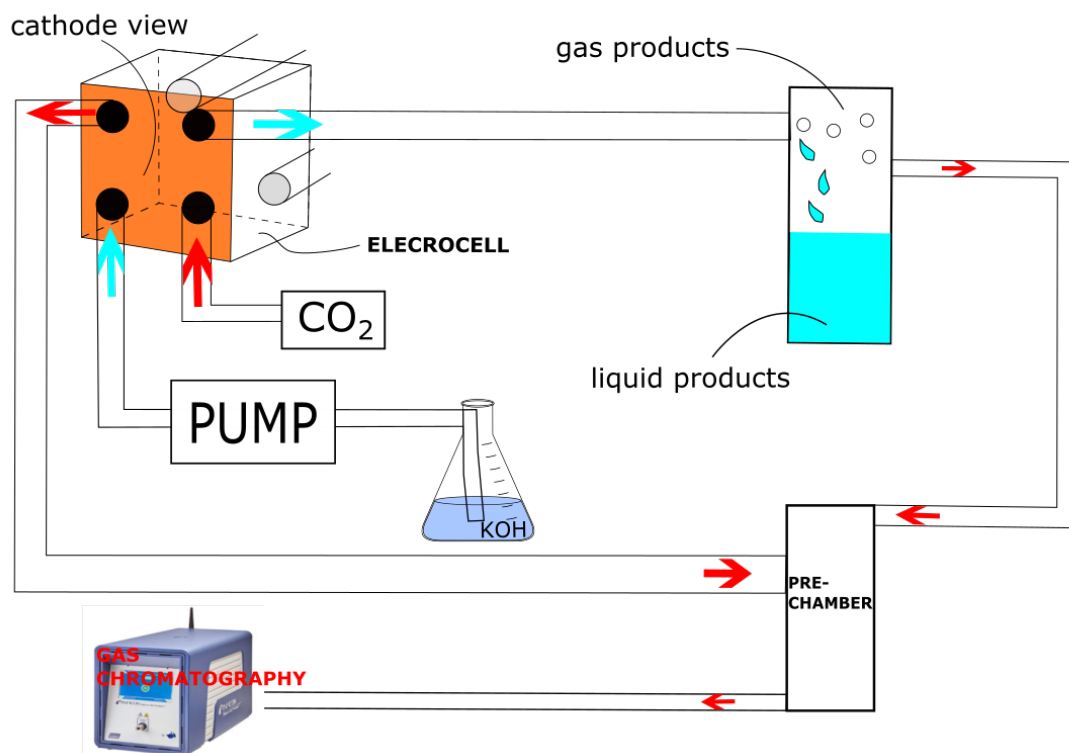

Figure 2.5: Membrane-based flow reactor

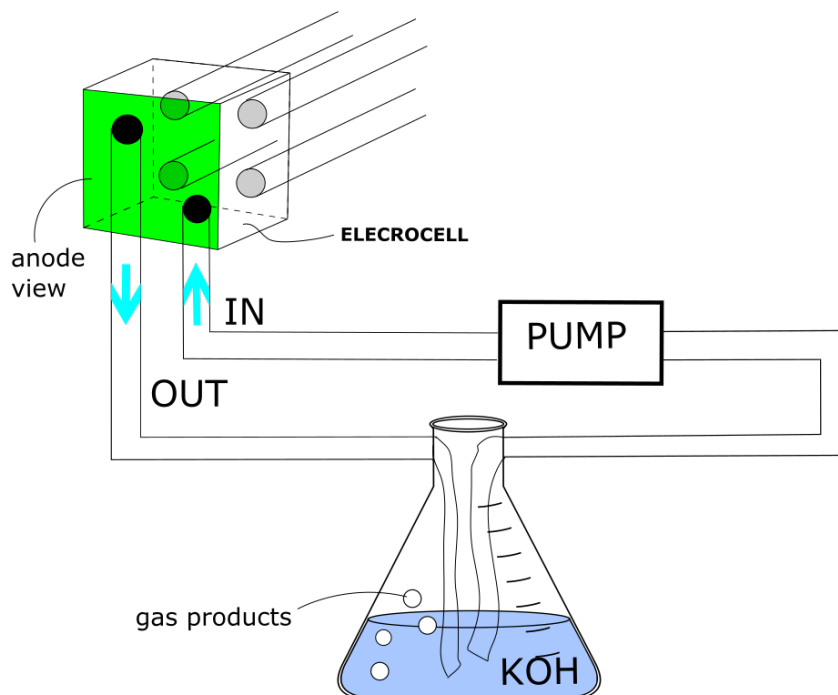Figure 2.6: Cathode view of the setup with KOH electrolyte

Figure 2.7: Anode view of the setup with KOH electrolyte

2.2.2 High Performance Liquid Chromatography

High Performance Liquid Chromatography (HPLC) is a technique used to separate different components contained in a liquid solution and quantify the concentration of each component.
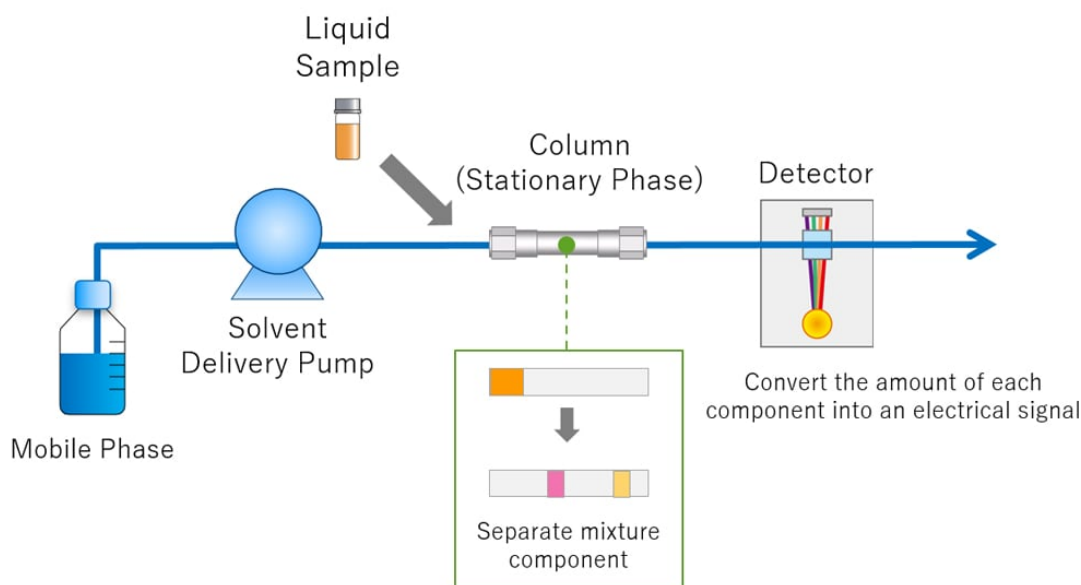The schematic is shown in Figure 2.8:

Figure 2.8: HPLC schematic
source by: https://www.shimadzu.com/an/sites/shimadzu.com.an/files/d7/
ckeditor/an/hplc/support/basic/what_hplc/1.jpg

There is a mobile phase that is injected in the column thank to a delivery pump that regulates the flow rate (matched with the detector). Before reaching the column, the liquid sample is mixed with the mobile phase thanks to an injector. At this point, due to different affinities with the stationary phase (the column), the analytes are separated. So when they are eluted from the column, they can be identified and quantified from the detector (Figure 2.9).
At this point the information of this analysis can be read from the chromatogram (Figure 2.10): the retention time (tR) is the time interval between the time of injection of the liquid solution into the column and the apex of the peak; instead the dead time (t0) is the time for a non retained compound (i.e. no interaction with the stationary phase) to travel from the injector to the detector.

To perform HPLC, ThermoFischer Ultimate 3000 was used. With a UV-Vis detector set at 210 nm by using a Reprogel H+ column (300 x 8 mm), with 9 mM H2SO4 (flow rate of 1.0 mL min-1) as mobile phase.
The FE related to liquid products in catholyte samples, taken at the beginning of each CP test, was calculated using Equation 2.3
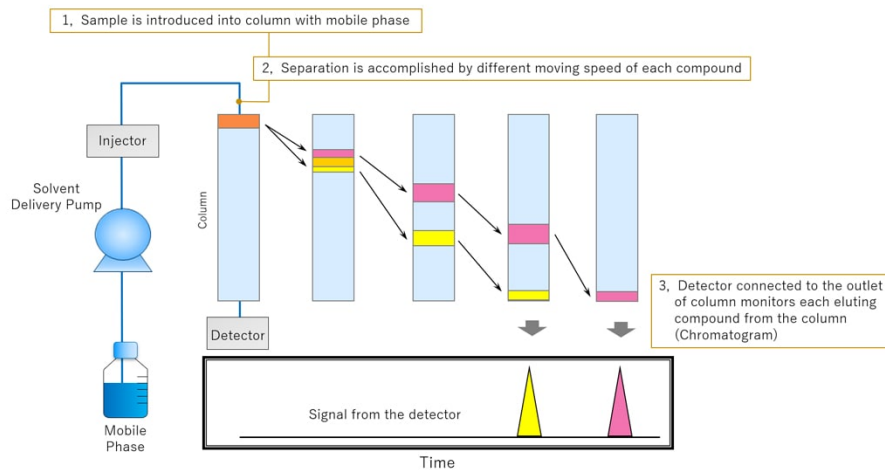
Figure 2.9: HPLC separation
source by: https://www.shimadzu.com/an/sites/shimadzu.com.an/files/d7/
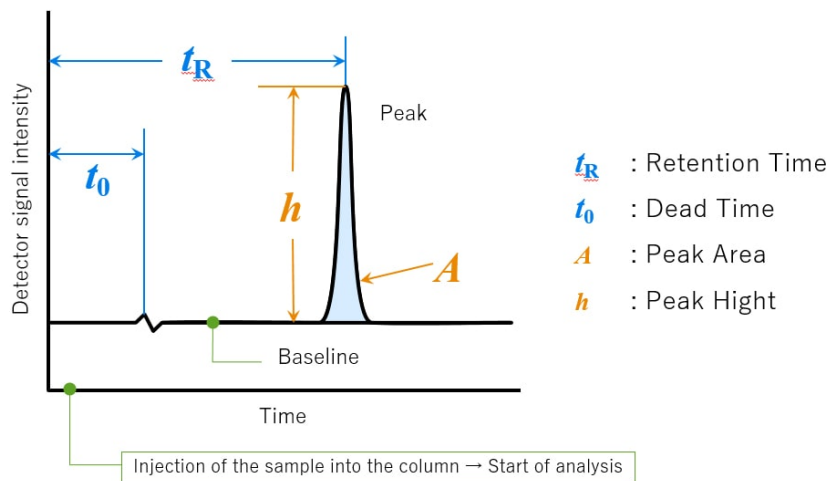ckeditor/an/hplc/support/basic/what_hplc/3.jpg

Figure 2.10: Chromatogram
source by: https://www.shimadzu.com/an/sites/shimadzu.com.an/files/d7/
ckeditor/an/hplc/support/basic/what_hplc/4.jpg

$$FE = \frac{\nu * C * n * F}{Q} \tag{2.3}$$

where ν is the volume of catholyte (L); C is the concentration of the liquid product $(mol L^{-1})$; n is the number of electrons required to obtain 1 molecule of this product; F is the Faraday constant (96485 $C mol^{-1}$); Q is the total charge passed through the system during the CP test (coulombs, C).

2.2.3   Gas chromatography

Gas chromatography (GC) is a technique used to separate components of a gas sample mixture and to perform a quantification of these components.
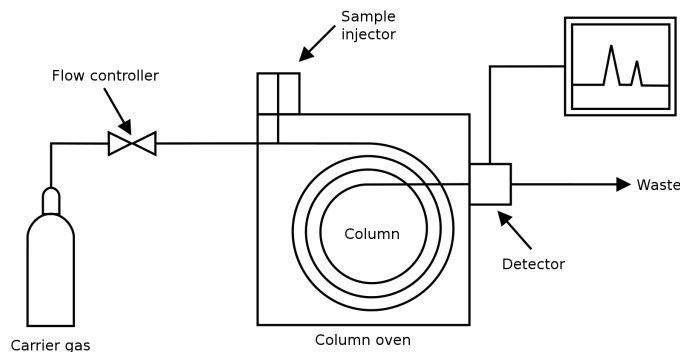

Figure 2.11: GC set-up

The sample is injected, with an inert carrier gas (the **mobile phase**), in the analytical column (fused silica or metal tube) that contains the **stationary phase**. During the analysis the column is heated in such a way to elute the chemical compounds and at the end they pass through a detector.

Chemical components are separated thanks to their different interactions with the stationary phase. In practice the detector identifies the different components as a function of time. The time spent by the analyte to stay in the stationary phase is called retention time (t_R). The time needed for a no retained analyte to travel through the column is called dead time (t_0). An important factor, that is used in the analysis, is the partition time:

$$k_n = t_R - t_0/t_0 \tag{2.4}$$

The separation factor between different analytes is defined as:

$$\alpha = k_2/k_1 \tag{2.5}$$

It is also important to have a quantification of the resolution (R) of the tool with the following formulas:

$$R = 1.18(t_{R2} - t_{R1})/(w_{h1} + w_{h2}) \tag{2.6}$$

$$R = 2(t_{R2} - t_{R1})/(w_{b1} + w_{b2}) \tag{2.7}$$

where t_{Rn} = retention times of peaks n; w_{hn} = peak width at half height of peaks n; w_{bn} = peak widths at the base of peaks n.

Gas-phase products were analyzed on-line with a micro gas chromatograph (μGC, Fusion®, INFICON). The μGC has two channels equipped with a 10 m Rt-Molsieve 5A column and a 8 m Rt-Q-Bond column, respectively, and each channel with a micro thermal conductivity detector (micro-TCD).

The FE value for each gas-phase product was determined from its concentration in the outlet gas of the cathodic compartment according to Equation 2.8

$$FE = \frac{V * t * C * n * F}{V_m * Q} \tag{2.8}$$

where V is the flow rate of CO_2 in the cathodic side ($25 L min^{-1}$); t is the electrolysis time (min); C is the concentration of the gas product (% v/v); V_m is the molar volume of an ideal gas ($L mol^{-1}$); n is the number of electrons required to obtain 1 molecule of this product; F is the Faraday constant ($96485\ C mol^{-1}$); Q is the total charge passed through the system during the electrolysis time t (coulombs, C).

2.2.4   Cyclic Voltammetry

To investigate the redox process of molecular species a common technique is Cyclic Voltammetry (CV). This type of process is commonly used to study electron transfer-initiated chemical reactions. A typical schematic of this type of experiment is shown in Figure 2.12 [51].
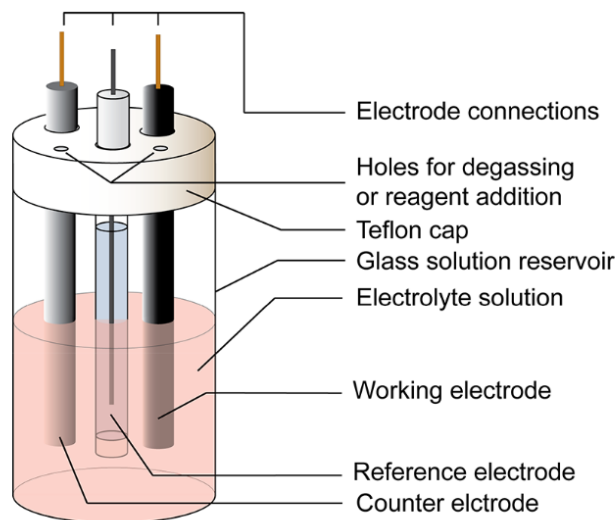

Figure 2.12: CV experiment. Image from [51]

Supplying a voltage source, the current will have the contribution of electrons and ions in the electrolyte solution to close the circuit. A typical plot of a CV experiment is shown in Figure 2.13 [51].

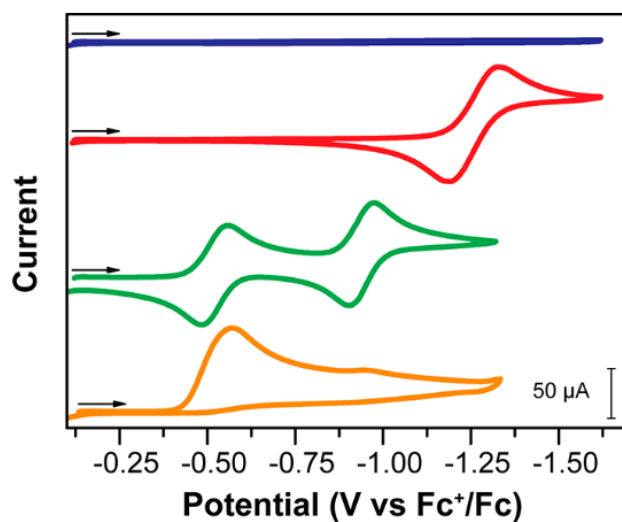Figure 2.13: Cyclic Voltammetry typical plot [51]

The lines in Figure 2.13 are called voltammograms or cyclic voltammograms. In the x-axis there is the applied potential; in y-axis there is the current. To understand

why there are peaks in a voltammograms, we can just look at the Nernst equation that connects the electrode potential (E) to the standard potential (E^0) and to the relative activities of ions in the solution [51].

$$E = E^0 + \frac{RT}{nF} ln \frac{(Ox)}{(Red)} \tag{2.9}$$

in eq.(2.9) F = Faraday's constant, R = universal gas constant, n = number of electrons, and T = temperature.

So peaks are connected to oxidation and reduction processes that change the potential of the electrode. The convention used for this project is the following:
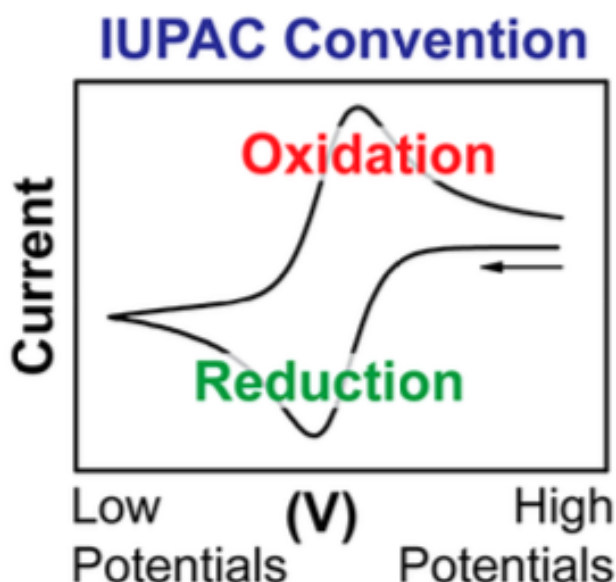

Figure 2.14: IUPAC convention [51]

Double layer capacitance

The double layer capacitance (C_{DB}) is related to the double layer of opposite charges, formed one at the electrode surface and one in the electrolyte. Solvent molecules, that adhere at the surface of the electrode, can be considered as a dielectric in a common capacitor (Figure 2.15). C_{DB} is an important parameter because it is proportional to the accessible surface area of the electrolyte ions.
When the electrode is supplied with a voltage ramp (scan rate (ν)), a steady-state capacitive current (i_c) is present if the only effect is the charging of the double layer (i.e. no redox processes involved). In this way a double layer capacitance can be evaluated from the slope of the $i_C - vs - \nu$ plot:
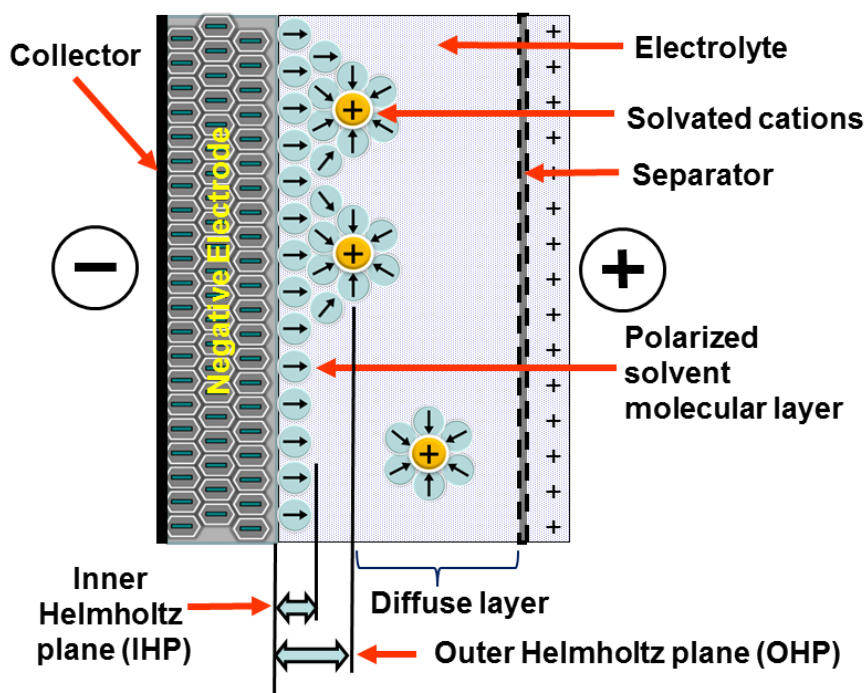
Figure 2.15: Double layer capacitance

$$i_C = \nu * C_{DB} \tag{2.10}$$

CV measurements were performed with a CH 700E Series Bipotentiostat at room temperature with a three electrodes cell as shown in Figure 2.12. A platinum wire was used as counter electrode. Ag/AgCl electrode was used as reference. The electrolyte used is KOH 1M saturated with N_2. To create the working electrodes, a square of 0.25 cm^2 was cut out from the fabricated GDEs and attached to a copper tape (Figure 2.16)

Figure 2.16: GDE electrodes tested with CV measurements

2.2.5 Electrochemical impedance spectroscopy

Electrochemical impedance spectroscopy (EIS) is used to study materials in which ionic conduction is prevalent on the electronic one (i.e when electrolytes are present in the system). During EIS, an AC voltage is applied to the system and the corresponding AC current is recorded. This technique can be done with 2 or 3 electrode configuration [52].

Electrochemical systems are usually not linear, but a pseudo-linear approximation can be acceptable if the amplitude of the AC voltage stimulus is low. The analytical formulation that can be done is the following: considering a sinusoidal voltage input $V(\omega, t) = V_0 sin(\omega t)$ (where V_0 is the amplitude of the input signal and ω is related to the chosen frequency f with the following equation: $\omega = 2\pi f$). The recorded response current at the same frequency is $I(\omega, t)$ and if the characteristic equation of the system is well known (i.e for resistor, capacitor and inductor), it can be derived from the theory. Finally the impedance (Z) of the system is just the ratio between the voltage and the current:

$$Z(\omega, t) = \frac{V(\omega, t)}{I(\omega, t}$$ (2.11)

If the voltage is a sinusoidal function, as mentioned above, $I(\omega, t)$ is also a sinusoidal one but, in general, it can be out-of-phase if the impedance of the system under test is frequency dependent. To take into account this condition the analytical expression becomes:

$$I(\omega, t) = V_0 sin(\omega t - \theta)$$ (2.12)

Exploiting the complex relationships:

$$Z(\omega, t) = \frac{V(\omega, t)}{I(\omega, t} = \frac{V_0 e^{j\omega t}}{I_0 e^{j\omega t - \theta}} = |Z(\omega)| e^{j\theta}$$ (2.13)

$|Z(\omega)|$ is the impedance modulus and θ is the impedance phase.

With Eulero's formulas, it becomes:

$$Z(\omega, t) = |Z(\omega)|(cos(\theta) + jsin(\theta)) = Z'(\omega) + jZ''(\omega)$$ (2.14)

In this way modulus and phase of the impedance can be obtained:

$$|Z(\omega)| = \sqrt{Z'(\omega)^2 + jZ''(\omega)^2}$$ (2.15)

$$\theta = \tan^{-1}\frac{Z''}{Z'}$$ (2.16)

In addiction to the 3 basic components (Resistor, Capacitor and Inductor), in literature is possible to find other electrochemical models. The three most used ones

are the constant phase element (CPE), the Warburg impedance and the Warburg short impedance. The impedance of each element is shown in the table below:

Element	Symbol	Impedance
Resistor	R	R
Capacitor	C	$\frac{1}{j\omega C}$
Inductor	L	$j\omega L$
Constant phase element	Q	$\frac{1}{Q(j\omega)^{\beta}}$
Warburg	W	$\frac{W}{\sqrt{j\omega}}$
Warburg short	W_s	$R_d\sqrt{\frac{\omega_d}{j\omega}}\,tanh\left(\sqrt{\frac{j\omega}{\omega_d}}\right)$

Figure 2.17: Table from Adriano Sacco, 2017 [52]

EIS were performed in a three-electrode cell Figure 2.12 at room temperature with a CH 700E Series Bipotentiostat. EIS measurements were performed at various potentials vs. Ag/AgCl: 1.436V - 1.636V - 1.836V - 2.036V, that correspond to: 0.4V - 0.6V - 0.8V - 1.0V vs. RHE. The AC signal was: 10 mV of amplitude and $10^{-1} - 10^5 Hz$ frequency range in a N_2 saturated 1M KOH aqueous solution.

2.2.6 X-Ray diffractometry

X-Ray Diffraction (XRD) is a common technique used to determine crystalline structure and atomic spacing. The basic principle of XRD is the constructive interference of monochromatic X-rays and a crystalline sample:
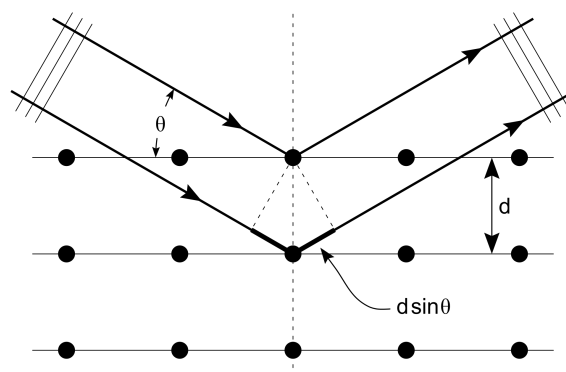

Figure 2.18: X-Ray diffraction

A cathode tube generates x-ray photons, that are filtered to obtain a monochromatic wave. When the x-ray photon impinges against the sample and the Bragg's

law is satisfied (eq. 2.17), there is a constructive interference and we see a peak in the XRD plot.

$$n\lambda = 2dsin\theta \tag{2.17}$$

Looking at this law it is easy to see the simple relation between the diffraction angle θ, the wavelength λ and the lattice spacing d. So scanning the sample in a range of different angles it is possible to identify the crystalline materials of the sample.

Chapter 3

Results and discussion

This section shows the results that came from the methods described in Chapter 2.
XRD results are related to electrodes with loading equal to $3.0mg * cm^{-2}$.
Chronopotentiometry results are related to all loadings; more current densities were
also applied at that electrodes with loading equal to $1.0mg*cm^{-2}$ and 25nm particles
size. Chronopotentiometry results with different substrate compositions are also
shown.
CV and EIS results are related to all loadings.

3.1   XRD (Cu 25nm)

Figure 3.7 represents the results of XRD of a Cu electrode with copper particles diameter of 25nm and loading equal to 3.0 $mg * cm^{-2}$. This electrode was deposited on a GDL substrate (Section 2.1). Cu electrode is compared with just only the GDL substrate. It is possible to see that peaks related to Cu presence are well defined. It is also possible to see a small presence of Cu_2O.
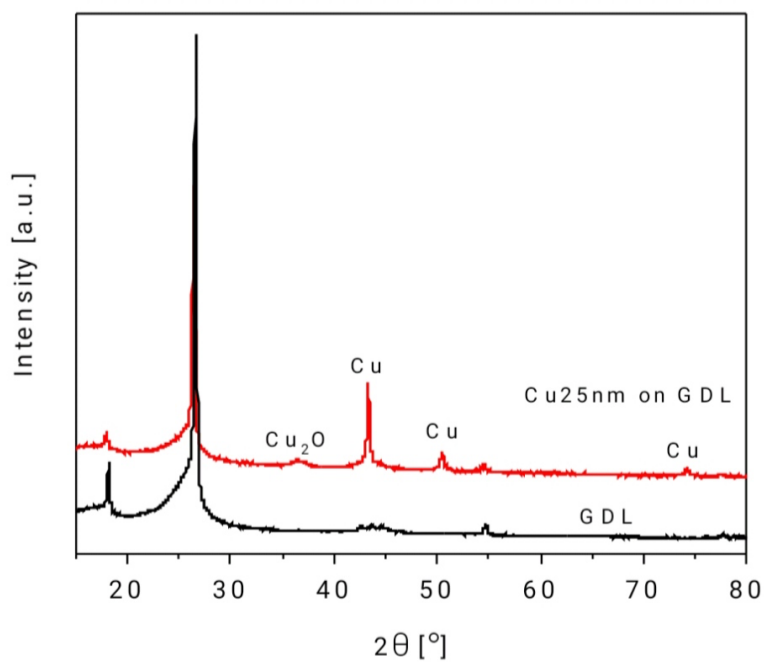
Figure 3.1: XRD - 25 nm 3.0 $mg * cm^{-2}$

3.2 XRD (Cu 50nm)

Figure 3.7 represents the results of XRD of a Cu electrode with copper particles diameter of 50nm and loading equal to 3.0 $mg*cm^{-2}$. This electrode was deposited on a GDL substrate (Section 2.1). Cu electrode is compared with just only the GDL substrate. It is possible to see that peaks related to Cu presence are well defined, but there are also more peaks, with respect to Cu 25nm, related to the presence of Cu_2O. This probably can be related to the bigger particles size that can induce an easier oxidation process with respect to Cu 25nm.
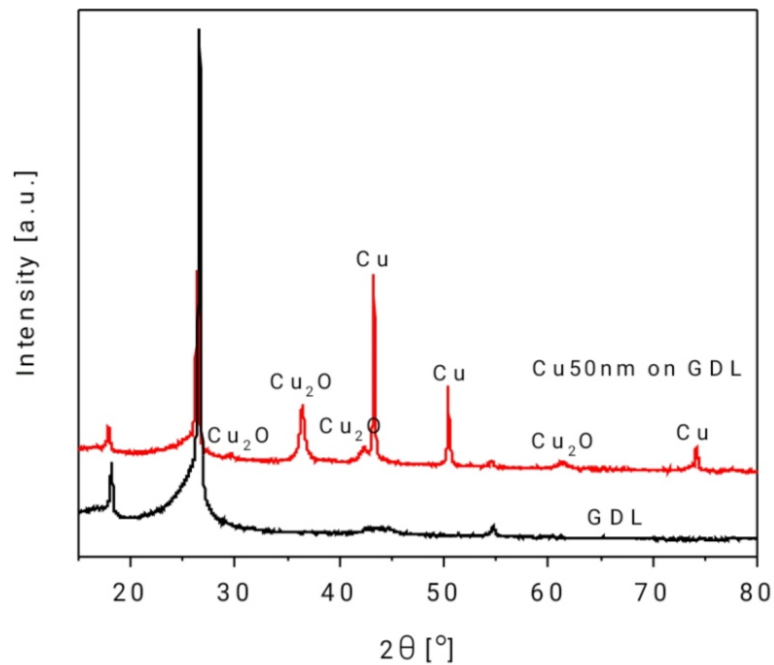
Figure 3.2: XRD - 50 nm 3.0 $mg*cm^{-2}$

3.3 Chronopotentiometry Cu 25 nm

Figure 3.3 and Figure 3.4 show the typical potential curves during the test of a 25 nm Cu electrode with loading $= 0.5mg * cm^{-2}$. The potential of the working electrodes was recorded at 2 different current densities: $200mA * cm^-2$ and $267mA * cm^-2$ respectively. On the right side of each figures is also shown the corresponding product analysis of micro-gas chromatography. We can see that the recorded potential, without iR compensation, is similar in both cases $\sim$ -1.3/-1.4 V vs. RHE.
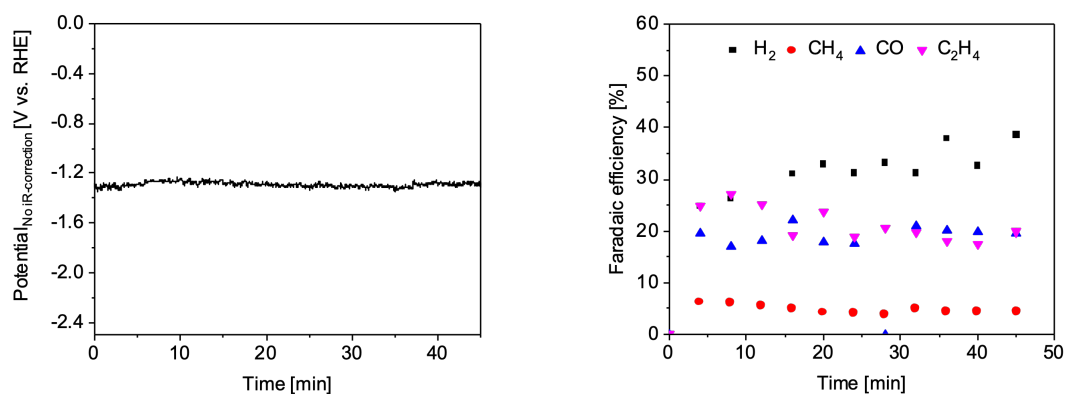
Figure 3.3: Potential curve and micro-gas chromatography at a constant current density of $200mA * cm^{-2}$
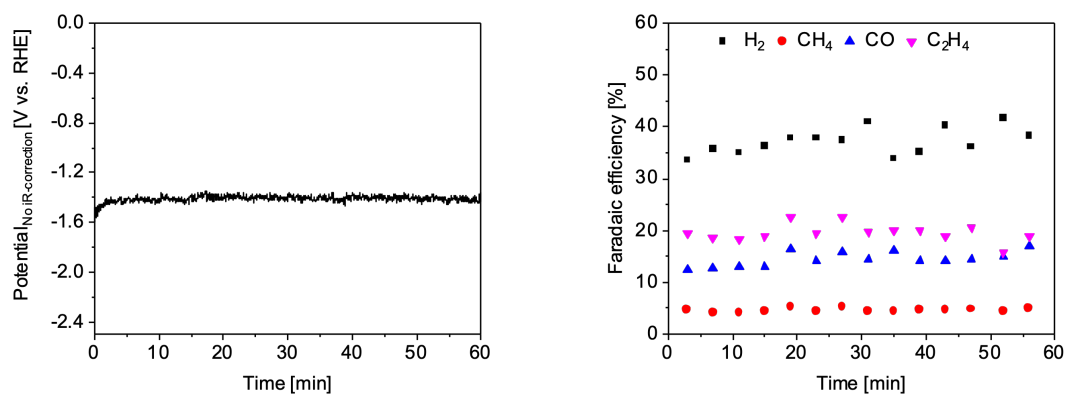
Figure 3.4: Potential curve and micro-gas chromatography at a constant current density of $267mA * cm^{-2}$

The figures below show the value of faradaic efficiencies at 2 different current densities (200 $mA*cm^{-2}$ and 267 $mA*cm^{-2}$) and for 6 different loadings of 25nm Cu electrode: $0.125mg*cm^{-2}$; $0.25mg*cm^{-2}$; $0.5mg*cm^{-2}$; $1.0mg*cm^{-2}$; $2.0mg*cm^{-2}$; $3.0mg*cm^{-2}$.
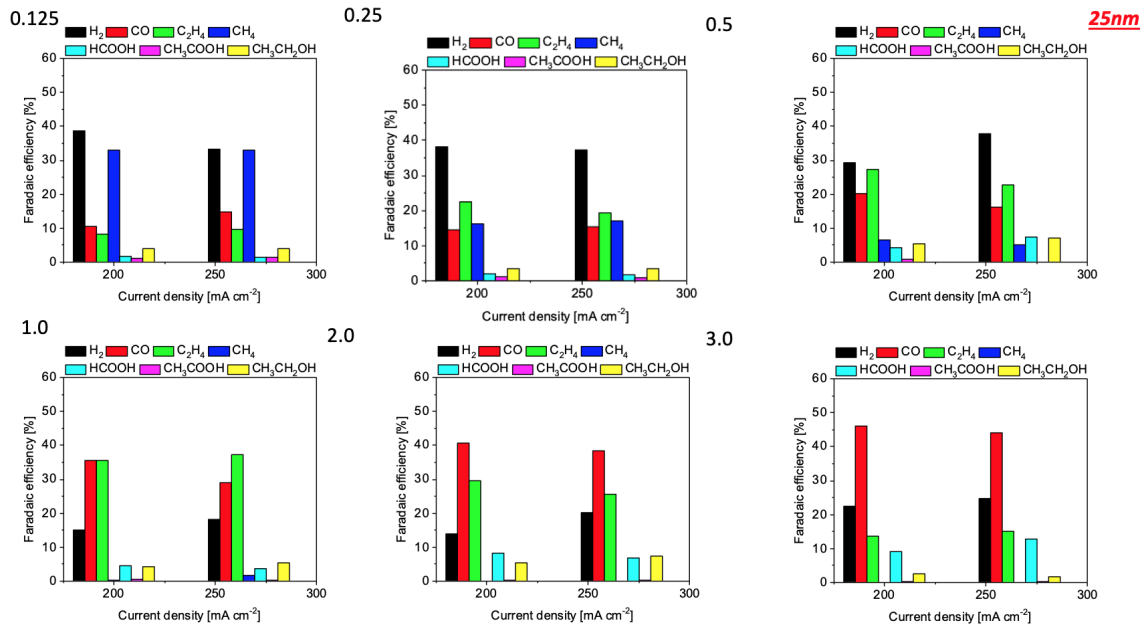

Figure 3.5: FE Cu 25nm

The results show that H_2 and CH_4 concentration decreases with the increasing of the loading, CO concentration increases with the loading, and C_2H_4 reaches the maximum of concentration for loading $= 1.0mg*cm^{-2}$.

Figure 3.6 shows the FE for the main products (FE CH_3COOH < 1.3%; FE $CH_4 < 3.1\%$, FE HCOOH < 5.0%) at different current densities for 25nm Cu with loading $= 1.0mg * cm^{-2}$. The results indicate that H_2 FE has a maximum for low current densities; CO FE decreases with raising the current density; C_2H_4 FE has a maximum for medium current density and C_2H_5OH FE increases with the current density.
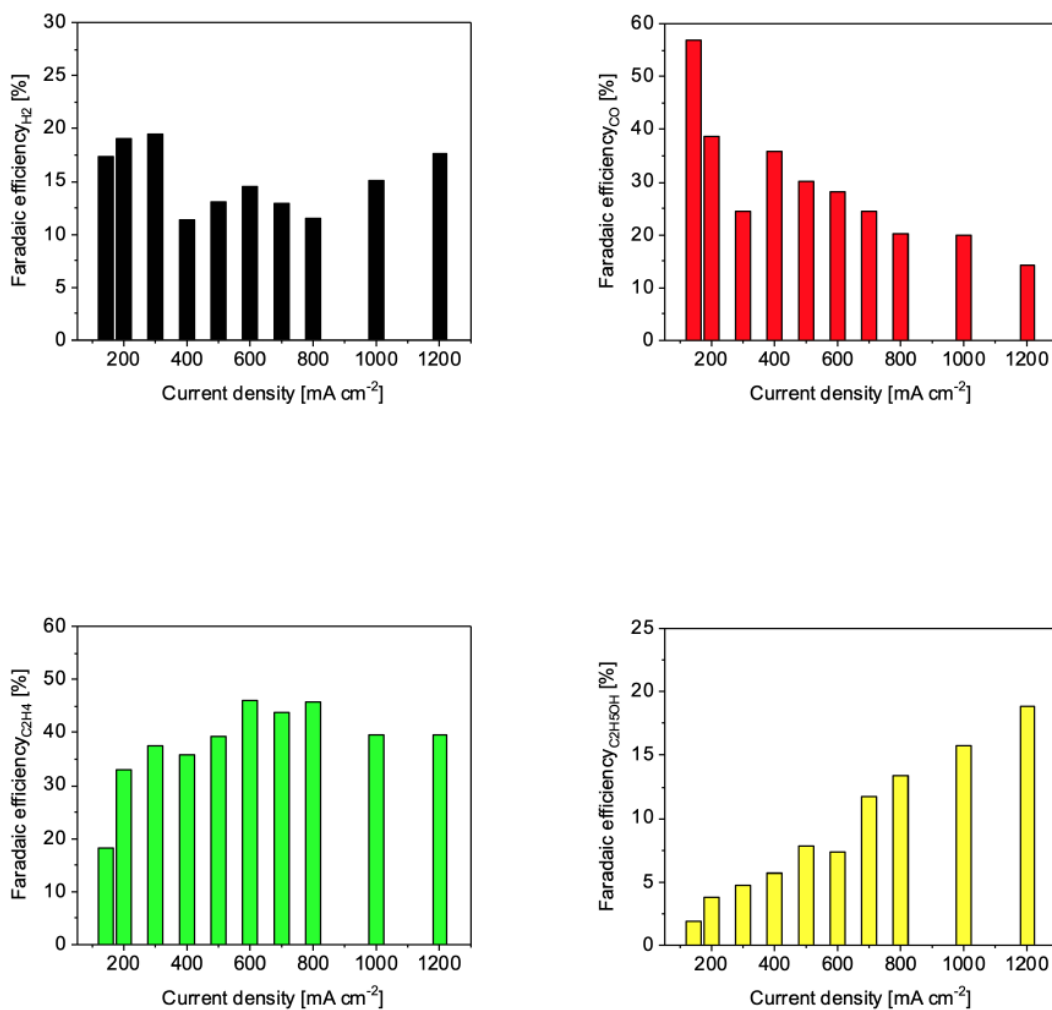

Figure 3.6: FE for H_2, CO , C_2H_4 and C_2H_5OH

Figure 3.7 shows the increasing of the cell voltage for the increasing of the current density. The cell voltage is the potential difference between the anode and cathode, and measured with two-electrode configuration. It can be seen that the voltage is relatively low even at high current densities > 1 A cm-2.
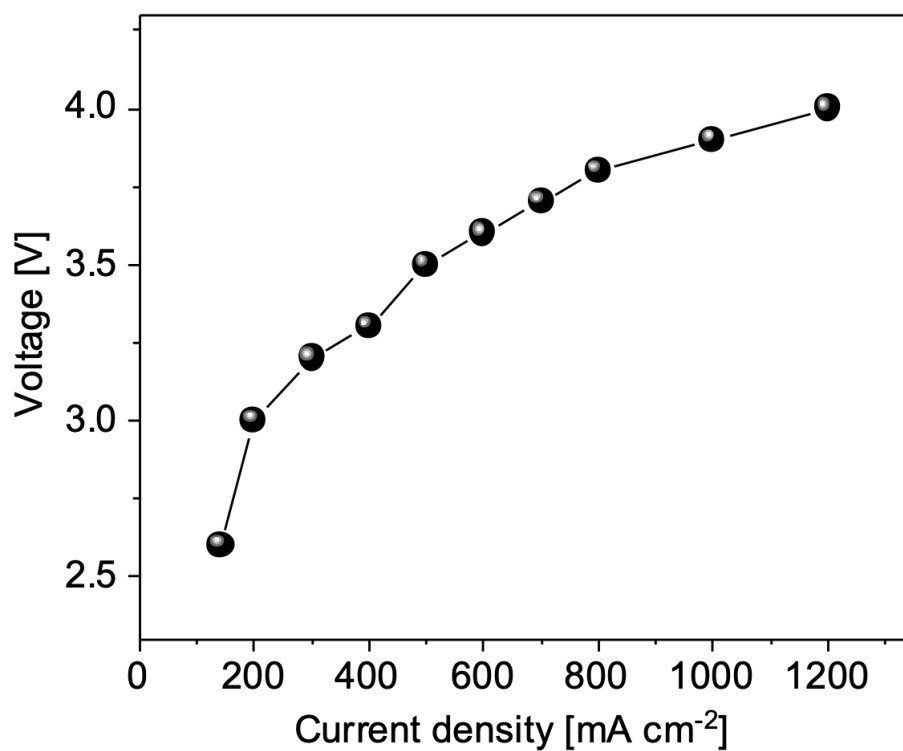

Figure 3.7: Cell voltage vs. current density

3.4 Chronopotentiometry Cu 50 nm

Figure 3.8 and Figure 3.9 show the typical potential curves during the test of a 50 nm Cu electrode with loading $= 0.5mg*cm^{-2}$. In this case the potential recorded is higher with respect to Cu 25nm. The potential is around: -1.05 V/ -1.18 V respectively.
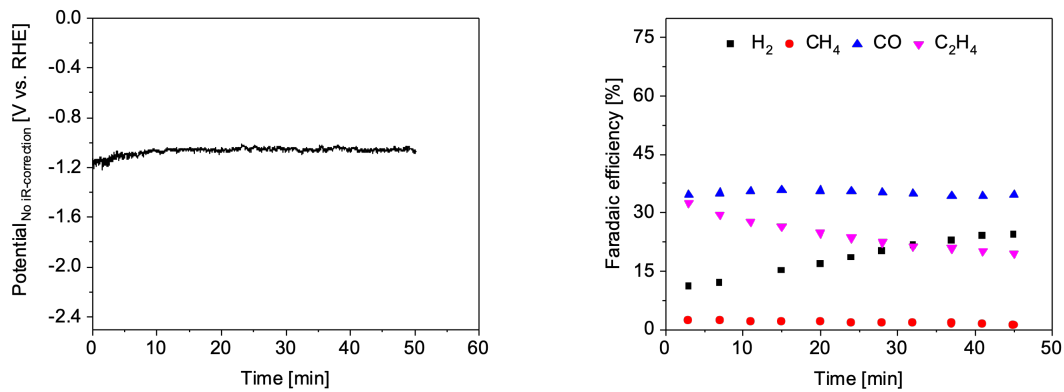

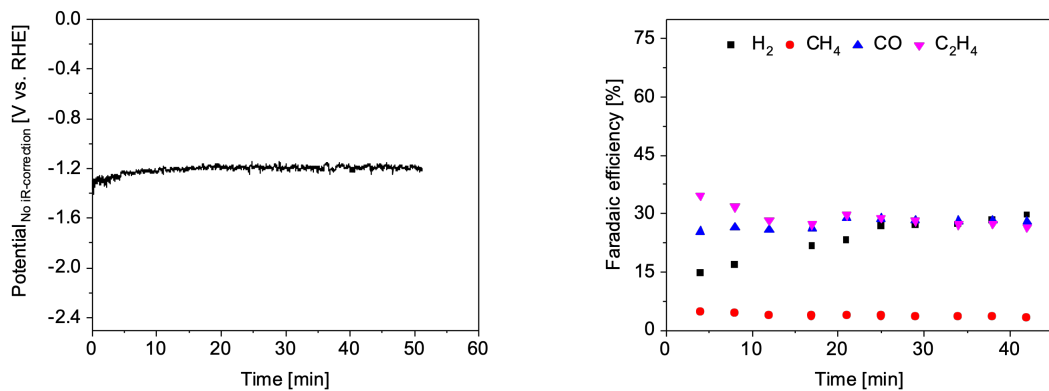Figure 3.8: Potential curve and micro-gas chromatography at a constant current density of $200mA*cm^{-2}$

Figure 3.9: Potential curve and micro-gas chromatography at a constant current density of $267mA*cm^{-2}$

The figures below show the value of faradaic efficiencies at 2 different current densities (200 $mA*cm^{-2}$ and 267 $mA*cm^{-2}$) and for 6 different loadings of 50nm Cu electrode: $0.125mg*cm^{-2}$; $0.25mg*cm^{-2}$; $0.5mg*cm^{-2}$; $1.0mg*cm^{-2}$; $2.0mg*cm^{-2}$; $3.0mg*cm^{-2}$.
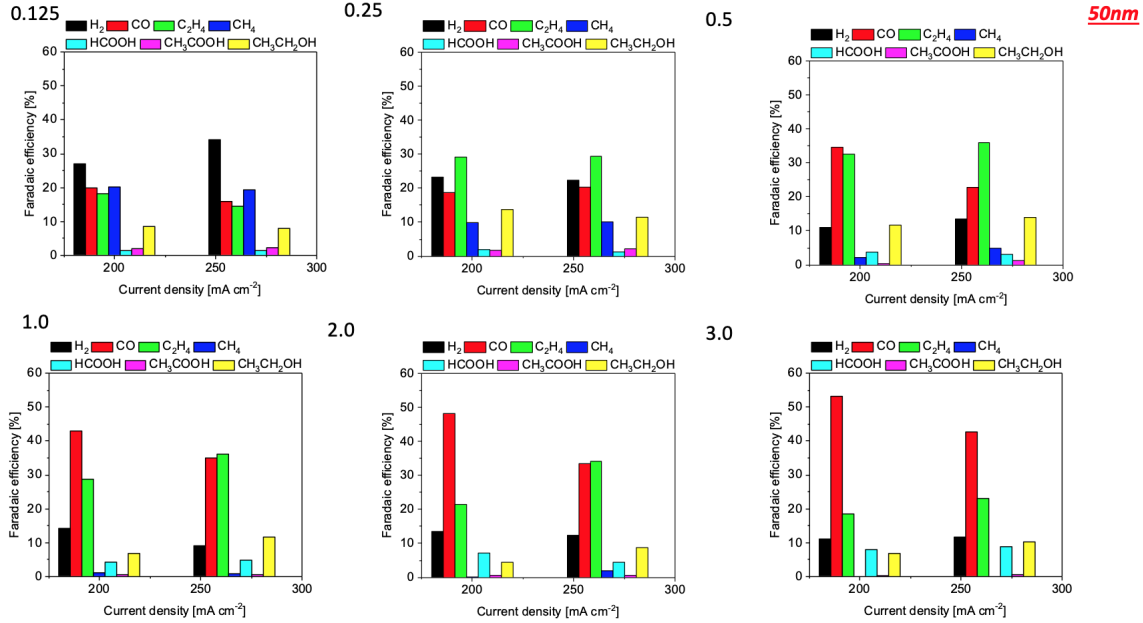

Figure 3.10: FE Cu 50nm

From this results it is possible to see that H_2 and CH_4 concentration decreases with the increasing of the loading. On the contrary CO concentration increases with the increasing of the loading. C_2H_4 reaches the maximum for loading = $1.0mg*cm^{-2}$. So the trend is consistent with that observed on Cu 25nm electrodes. Differences appear more evident at low loading values: Cu 25nm is more selective for H_2 and CH_4, whereas Cu 50nm is more selective for C_2H_4 and CO.

3.5 Chronopotentiometry varying GDL substrate composition

According to the previous results, Cu electrodes with $1.0mg*cm^{-2}$ show the best performance for the production of C_2H_4. For this reason this loading value was chosen to perform a stability test with Cu-25nm particles size, thus studying the effect of GDL substrates with different FEPD 121 compositions. The amount of FEPD 121 that was mixed with Vulcan XC-72R or Graphene particles was maintained at wt% values in the range of 20 wt% to 60 wt%. So samples compositions are: **baseline; 20%; 30%; 40%; 50%; 60%.**

Moreover tests were done at 2 different current densities: $300mA * cm^{-2}$ and $600mA * cm^{-2}$. Results are shown in the figures below.

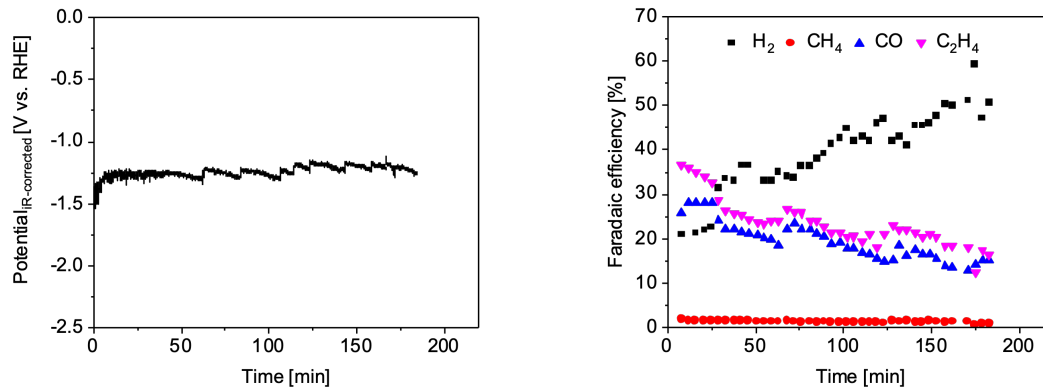

Figure 3.11: Baseline with $300mA * cm^{-2}$. Left: potential curve. Right: faradaic efficiencies.

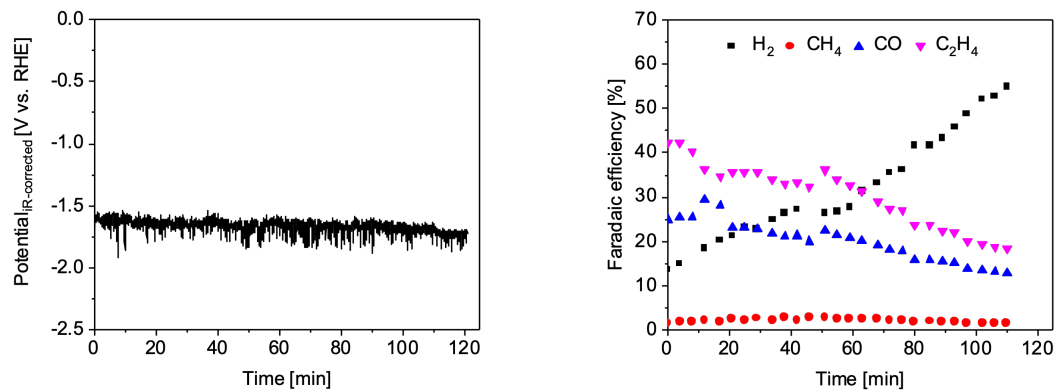Figure 3.12: Baseline with $600mA * cm^{-2}$. Left: potential curve. Right: faradaic efficiencies.

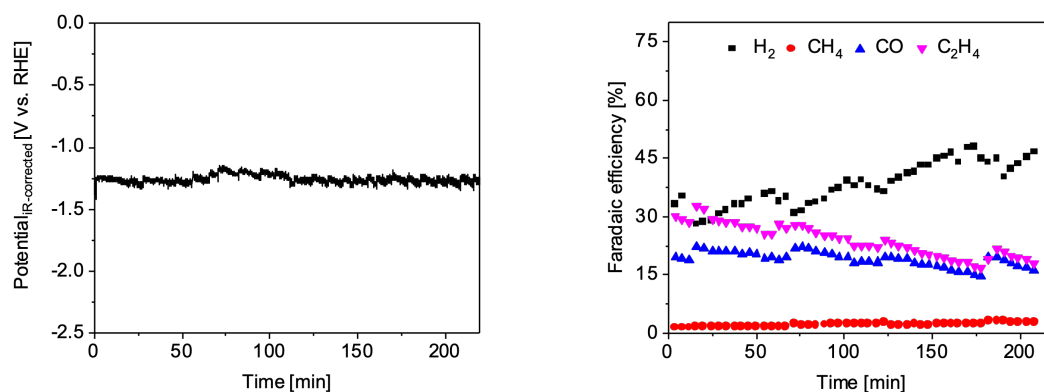Figure 3.13: 20% of FEPD 121 with $300mA * cm^{-2}$. Left: potential curve. Right: faradaic efficiencies.

Figure 3.14: 20% of FEPD 121 with $600mA * cm^{-2}$. Left: potential curve. Right: faradaic efficiencies.

Figure 3.15:   30% of FEPD 121 with $300 mA * cm^{-2}$. Left: potential curve. Right: faradaic efficiencies.

Figure 3.16:   30% of FEPD 121 with $600 mA * cm^{-2}$. Left: potential curve. Right: faradaic efficiencies.
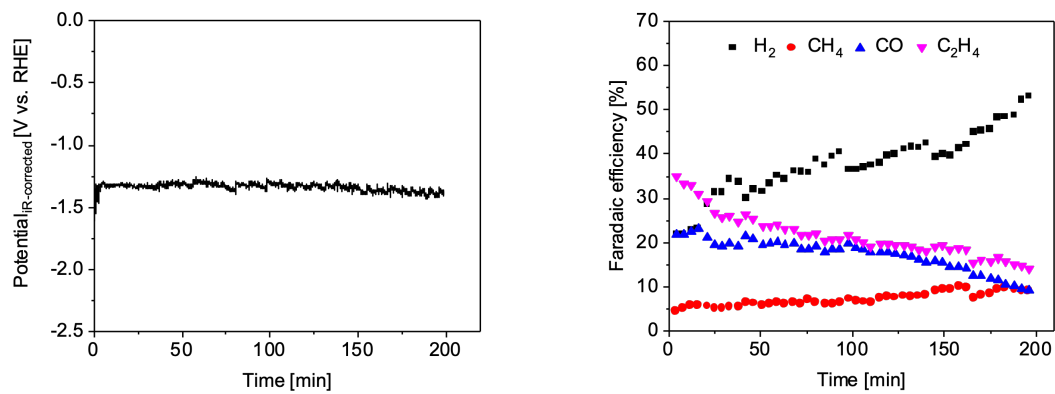
Figure 3.17: 40% of FEPD 121 with $300 mA * cm^{-2}$. Left: potential curve. Right: faradaic efficiencies.
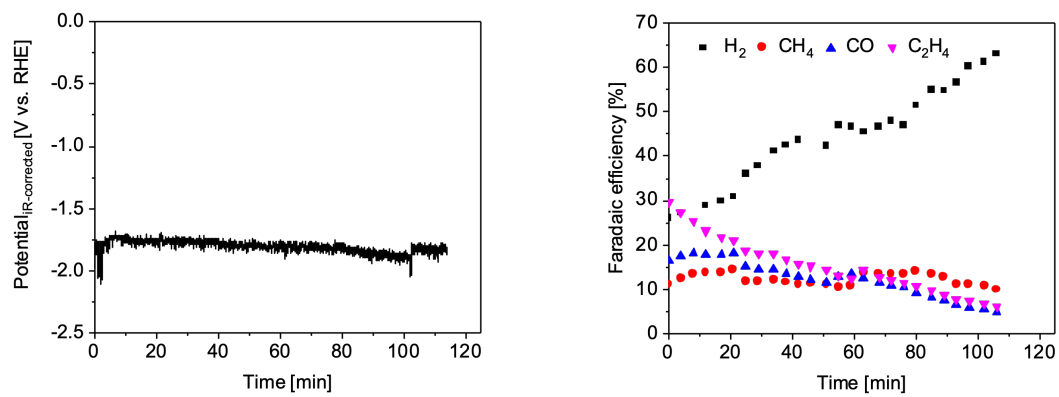
Figure 3.18: 40% of FEPD 121 with $600 mA * cm^{-2}$. Left: potential curve. Right: faradaic efficiencies.

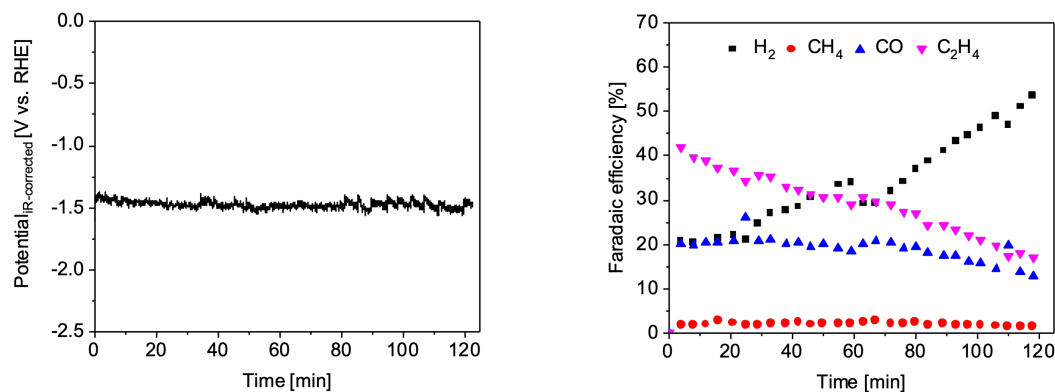Figure 3.19:   50% of FEPD 121 with $300mA * cm^{-2}$. Left: potential curve. Right: faradaic efficiencies.

Figure 3.20:   50% of FEPD 121 with $600mA * cm^{-2}$. Left: potential curve. Right: faradaic efficiencies.

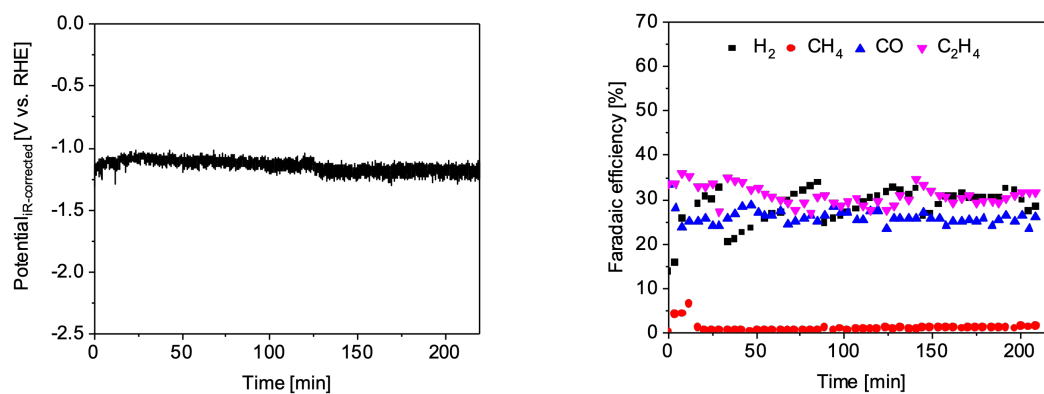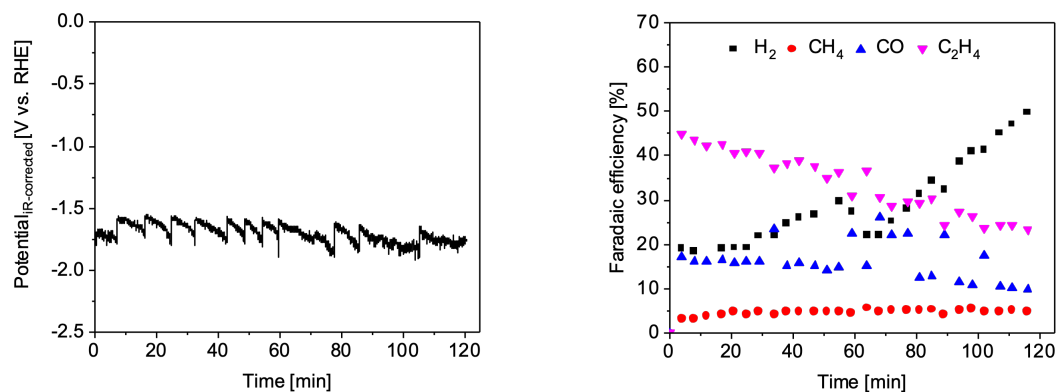Figure 3.21: 60% of FEPD 121 with $300mA*cm^{-2}$. Left: potential curve. Right: faradaic efficiencies.
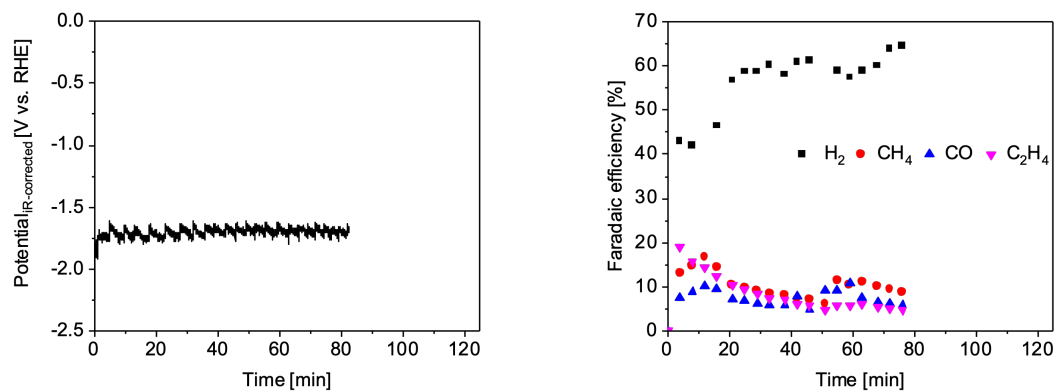
Figure 3.22: 60% of FEPD 121 with $600mA*cm^{-2}$. Left: potential curve. Right: faradaic efficiencies.

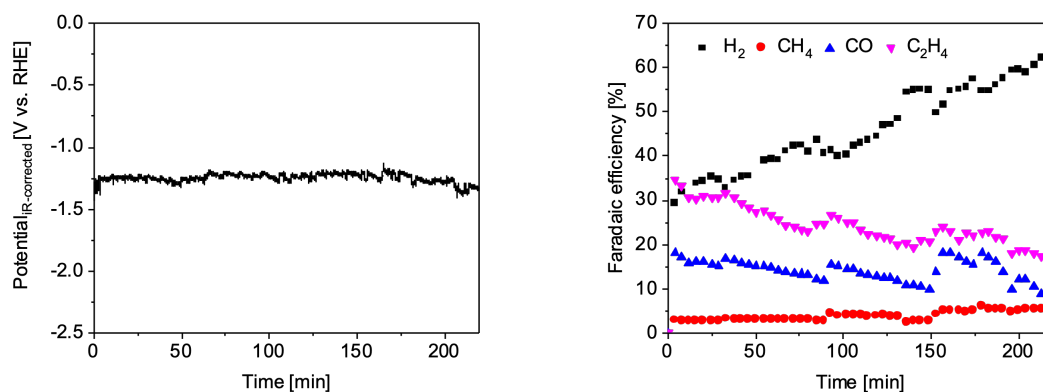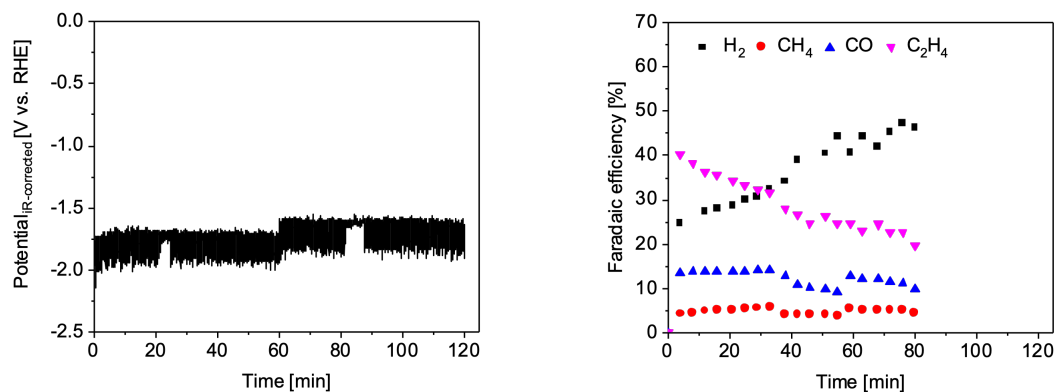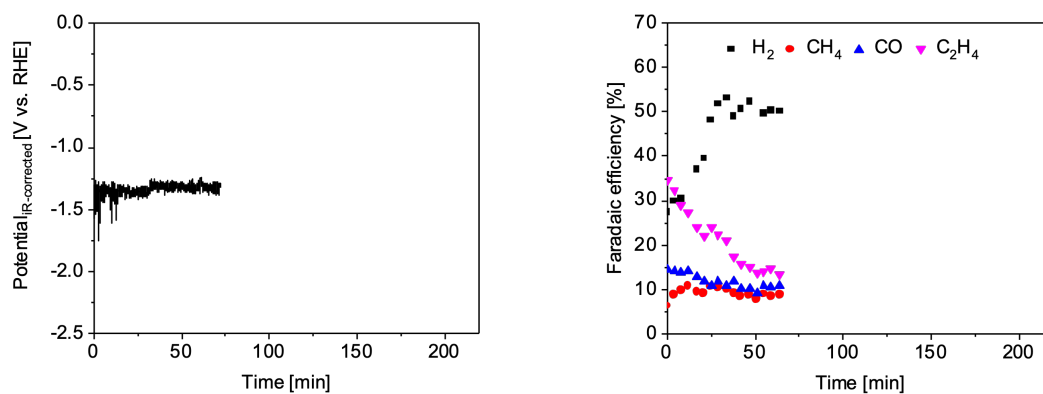According to these results the more stable substrate seems to be that one with 30% of FEPD 121 using a current density equal to $300mA*cm^{-2}$. The reached FE for C_2H_4 is larger than 30%.

3.6   Cyclic voltammetry 25nm

Figure 3.23 shows the typical cyclic voltammetry curves for different loadings of Cu 25nm. It is possible to see that for a higher loading the current involved is also higher due to the higher presence of Cu particles for the same geometric area ($0.25cm^2$).
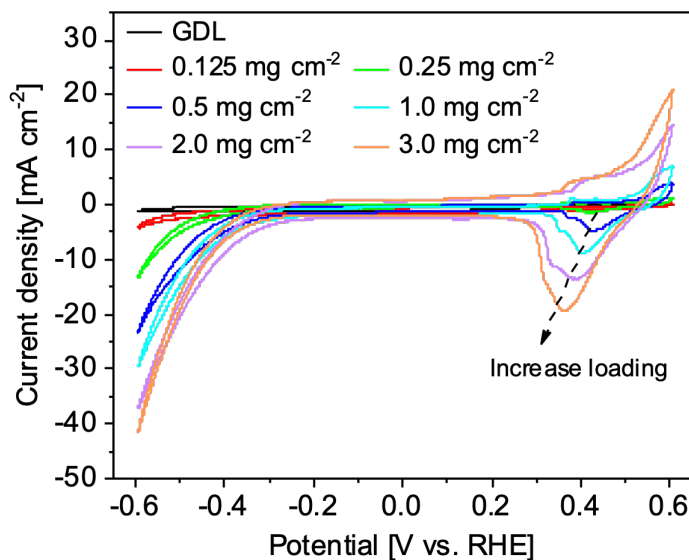
Figure 3.23: Cyclic voltammetry curve

Figure 3.24 shows how the C_{dl} was computed: on the left side, there is a zoom of the CV curve in the voltage window between 0 V and 0.25 V (where no redox reactions occur) for 25nm Cu with loading $= 0.125mg * cm^{-2}$; on the right side the current density, corresponding to $\sim 0.15V$ (round the center of the CV curve), was plotted versus the scan rate and the slope of the curve was calculated to obtain the double layer capacitance (C_{dl}).

In this way the corresponding C_{dl} at each loading was calculated and the results are in the table below.

LOADING $[mg * cm^{-2}]$	Double layer capacitance$(C_{dl})[mF * cm^{-2}]$
0.0 (GDL substrate)	1.6
0.125	2.8
0.25	1.4
0.5	2.1
1.0	2.7
2.0	7.4
3.0	7.8
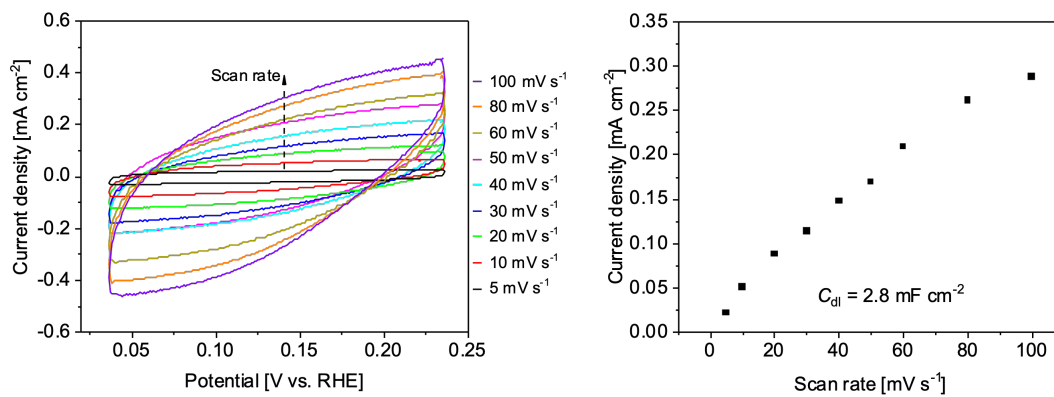
Figure 3.24: Method to evaluate the (C_{dl}) from the CV curve

3.7 Cyclic voltammetry 50nm

Figure 3.25 shows the typical cyclic voltammetry curve for different loadings of Cu 50nm.
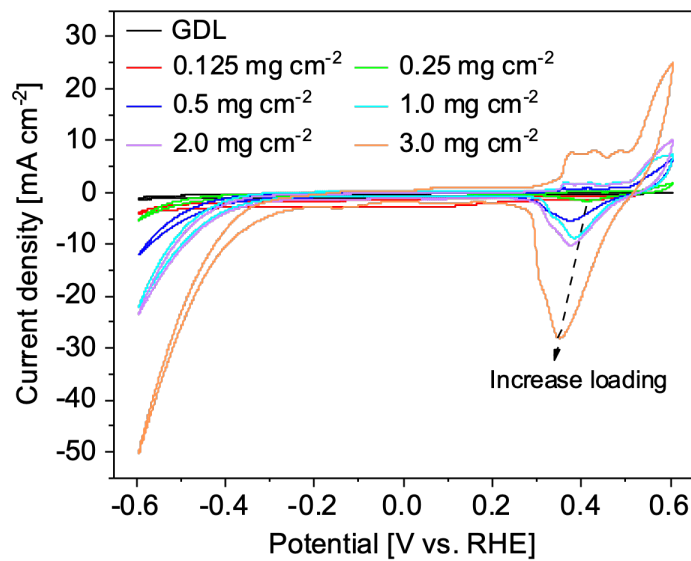
Figure 3.25: Cyclic voltammetry curve

Using the same method used for Cu 25nm we can calculate the C_{dl} for Cu 50nm and the results are in the table below.

LOADING $[mg*cm^{-2}]$	Double layer capacitance$(C_{dl})[mF*cm^{-2}]$
0.0 (GDL substrate)	1.6
0.125	2.8
0.25	1.2
0.5	2.0
1.0	3.0
2.0	3.5
3.0	8.6

3.8 C_{dl} for 25nm and 50nm

In Figure 3.26 the C_{dl} for Cu 25nm and 50nm, at different loadings, are shown:
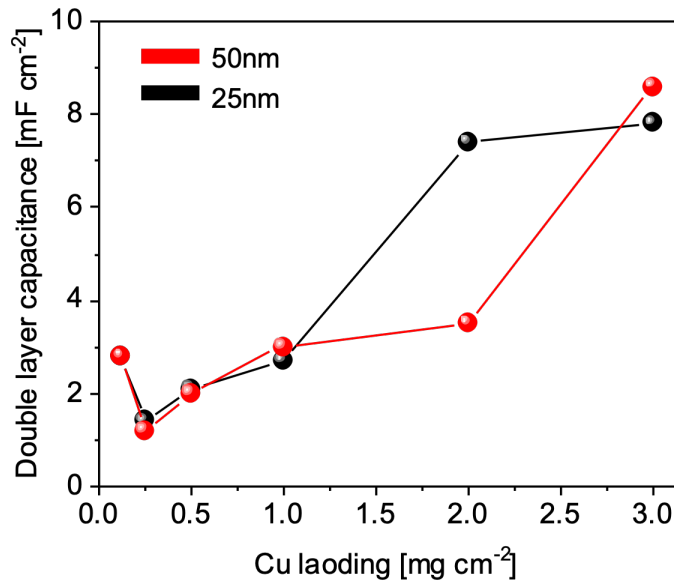
Figure 3.26: C_{dl} curves for 25nm and 50nm

In both, as expected due to the higher presence of active sites, there is an increase of C_{dl} value starting from 0.25 $[mg*cm^{-2}]$ but, the C_{dl} value corresponding to 0.125 $[mg*cm^{-2}]$ is unexpectedly higher than 0.25 $[mg*cm^{-2}]$ for both particles sizes. This outcome could be due to the big contribution of the substrate to the C_{dl} when the catalyst layer is very thin at extremely low loading.

3.9   Electrochemical impedance spectroscopy

In Figure 3.27 is shown an example of the Nyquist plots related to the impedance of a Cu-based electrode (red points). It is possible to recognize a two-time constant spectrum: the smaller arc is related to charge transport properties and the bigger one is related to charge transfer at the electrode/electrolyte interface. The corresponding electrical model is shown in Figure 3.28. In this model: Rs represents the electrolyte and contact resistances; Rt and Ct are related to the catalyst charge transport and Rct and Cdl are related to the charge transfer at the electrode/electrolyte interface [53]. By employing this circuit, it is possible to fit the experimental data, obtaining the fitting curve shown in Figure 3.27 (green line) and the best fit parameters related to each circuit element.
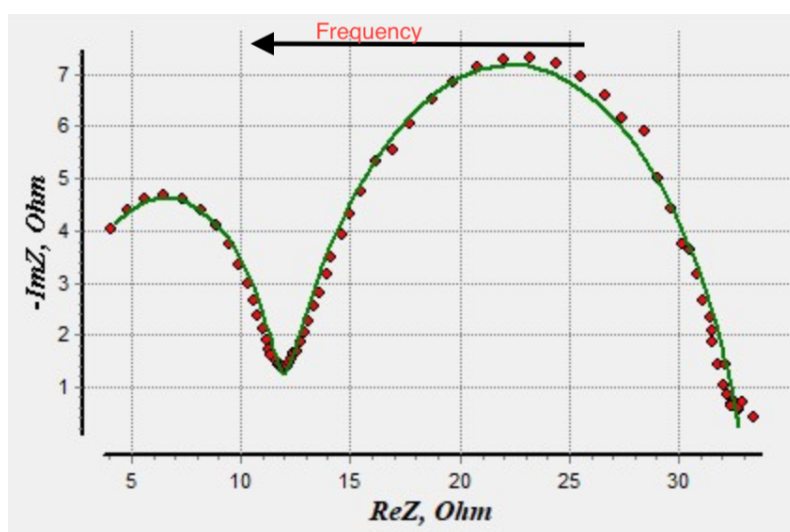
Figure 3.27: Typical EIS Nyquist plot
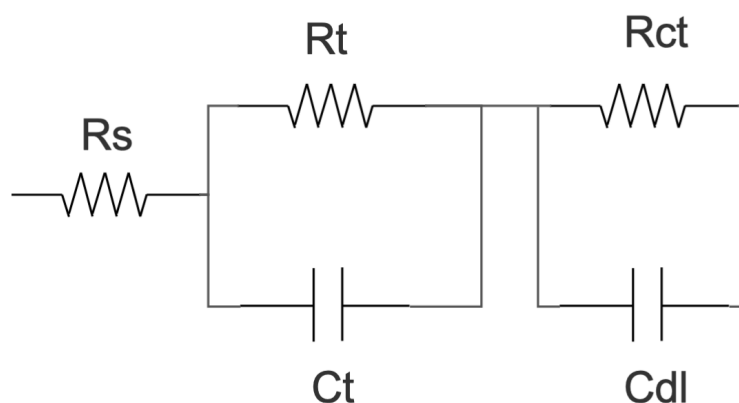
Figure 3.28: Electrical model

The values of Rs, Rt, Ct and Cdl (listed in the tables below) are equal to the arithmetic average of the corresponding values for each applied potential (-0.4V; -0.6V; -0.8V; -1.0V):

Sample ($mg * cm^{-2}$)	Rs ($\Omega * cm^2$)	Rt ($\Omega * cm^2$)	Ct (uF/cm^2)	Cdl (mF/cm^2)
GDL substrate	0.38	2.40	1.01	4.12
0.125-25nm	0.28	1.35	1.98	1.77
0.25-25nm	0.27	1.75	1.76	0.88
0.5-25nm	0.35	1.44	1.47	0.98
1.0-25nm	0.35	1.37	1.41	0.85
2.0-25nm	0.33	4.61	1.74	1.48
3.0-25nm	0.32	1.94	1.82	1.80
0.125-50nm	0.36	2.02	0.91	0.69
0.25-50nm	0.30	1.90	1.09	0.73
0.5-50nm	0.44	2.50	1.15	1.02
1.0-50nm	0.38	2.55	0.98	1.06
2.0-50nm	0.31	2.42	1.25	1.13
3.0-50nm	0.27	2.17	1.05	1.27

Rct values, for each applied potential, are shown in the figures Figure 3.29 and Figure 3.30. The charge transfer resistance value (Rct) is inversely proportional to the loading of the electrode and, using 50nm particles diameter, it reaches higher value with respect to 25nm one, indicating higher faradic reactions rates for the electrode with 25nm particles diameter. For this experiment a N_2 saturated electrolyte solution was used, this means that 25nm are more active for HER reaction and this is consistent with the chronopotentiometry results.
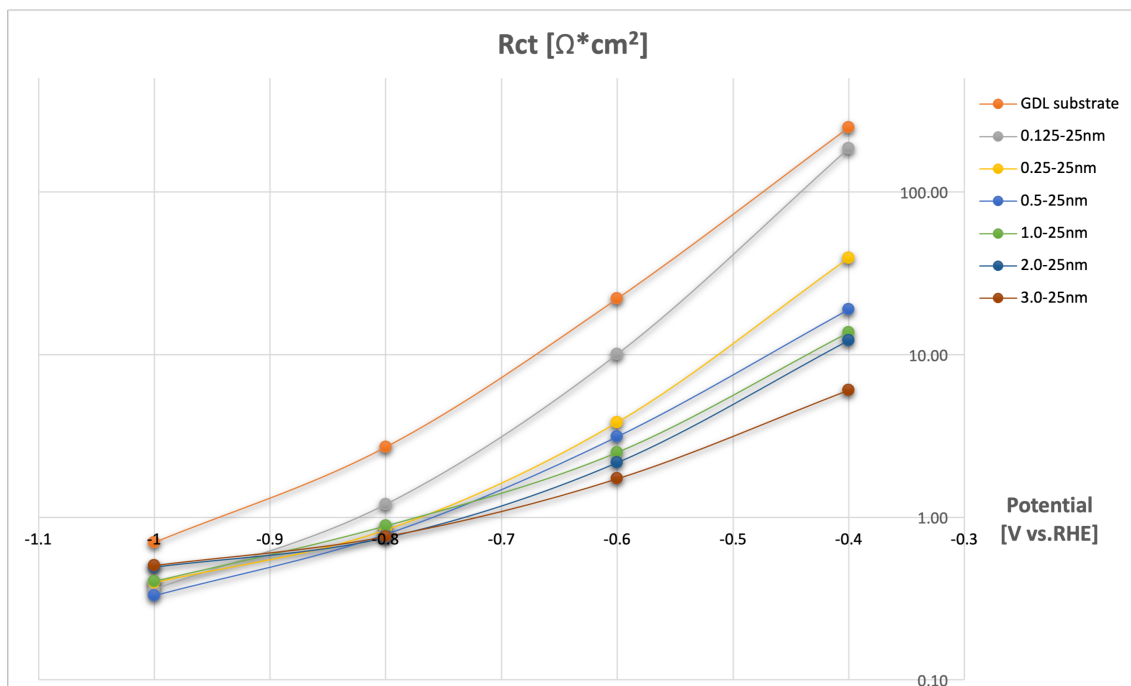
Figure 3.29: Rct values for 25nm samples
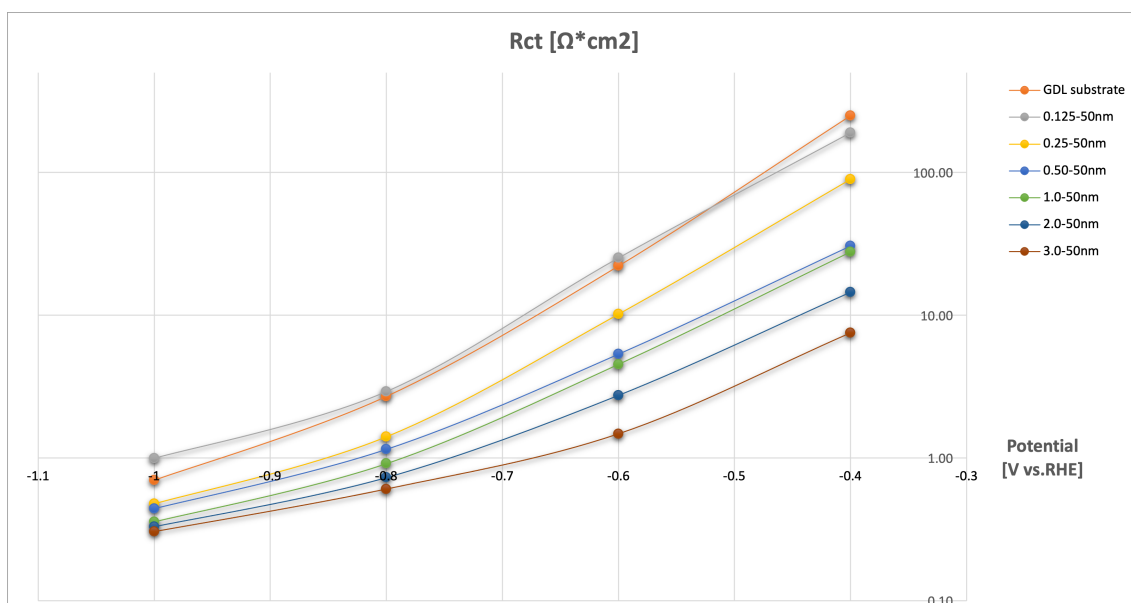
Figure 3.30: Rct values for 50nm samples

In conclusion Cu 25nm and Cu 50nm show more different results at low loadings. In this condition few particles are present on the surface of the electrode and they are well separated to each other, so the difference size at the nanoscale can cause different results especially in terms of faradaic efficiencies.

Chapter 4

Conclusions and future developments

Cu electrodes, deposited with drop-casting technique at different loadings, were prepared and studied for electrochemical CO_2 reduction. Moreover two different particles size diameters were used.

The results show that Cu-25nm is more selective for H_2 and CH_4 production, whereas Cu-50nm is more selective for CO and C_2H_4 at the same conditions. Both particles sizes reach a maximum FE value for C_2H_4 at loading equal to $1.0mg*cm^{-2}$. The stability test shows that a GDL substrate with 30% of FEPD 121 has the highest FE for C_2H_4 and better stability.

The CV study shows similar C_{dl} trend for both particles size, except for Cu loading $= 2.0mg*cm^{-2}$. Moreover at very low loading the used method fails, thus a CV study, using a flow cell system, could be more reliable.

EIS results are coherent with the higher HER activity of Cu-25nm with respect to that of Cu-50nm at the same conditions. Cu-50nm and Cu 25nm shows more different results at low loadings so more particles sizes should be studied at low loading to see if C_2H_4 FE can be improved.

Bibliography

[1] "Greenhouse effect — Wikipedia, the free encyclopedia," 2022.

[2] S. Jiao, X. Fu, L. Zhang, L. Zhang, S. Ruan, Y.-J. Zeng, and H. Huang, "The lab-to-fab journey of copper-based electrocatalysts for multi-carbon production: Advances, challenges, and opportunities," *Nano Today*, vol. 36, p. 101028, 2021.

[3] A. M. et al., "Theoretical insights into the factors affecting the electrochemical reduction of co2," *Sustainable Energy Fuels*, vol. 4, p. 4352, 2020.

[4] R. A. Tufa, D. Chanda, M. Ma, D. Aili, T. B. Demissie, J. Vaes, Q. Li, S. Liu, and D. Pant, "Towards highly efficient electrochemical co2 reduction: Cell designs, membranes and electrocatalysts," *Applied Energy*, vol. 277, p. 115557, 2020.

[5] Z. Xing, L. Hu, D. S. Ripatti, X. Hu, and X. Feng, "Enhancing carbon dioxide gas-diffusion electrolysis by creating a hydrophobic catalyst microenvironment," *Nature Communications*, vol. 12, no. 1, p. 136, 2021.

[6] Y. Zhou, F. Che, M. Liu, C. Zou, Z. Liang, P. De Luna, H. Yuan, J. Li, Z. Wang, H. Xie, H. Li, P. Chen, E. Bladt, R. Quintero-Bermudez, T.-K. Sham, S. Bals, J. Hofkens, D. Sinton, G. Chen, and E. H. Sargent, "Dopant-induced electron localization drives co2 reduction to c2 hydrocarbons," *Nature Chemistry*, vol. 10, no. 9, pp. 974–980, 2018.

[7] A. A. Peterson, F. Abild-Pedersen, F. Studt, J. Rossmeisl, and J. K. Nørskov, "How copper catalyzes the electroreduction of carbon dioxide into hydrocarbon fuels," *Energy Environ. Sci.*, vol. 3, pp. 1311–1315, 2010.

[8] Z. W. Seh, J. Kibsgaard, C. F. Dickens, I. Chorkendorff, J. K. Nørskov, and T. F. Jaramillo, "Combining theory and experiment in electrocatalysis: Insights into materials design," *Science*, vol. 355, no. 6321, p. eaad4998, 2017.

[9] C. Chen, J. F. Khosrowabadi Kotyk, and S. W. Sheehan, "Progress toward commercial application of electrochemical carbon dioxide reduction," *Chem*, vol. 4, no. 11, pp. 2571–2586, 2018.

[10] A. L. Soli and R. H. Byrne, "Co2 system hydration and dehydration kinetics and the equilibrium co2/h2co3 ratio in aqueous nacl solution," *Marine Chemistry*, vol. 78, no. 2, pp. 65–73, 2002.

[11] H. Zhong, K. Fujii, Y. Nakano, and F. Jin, "Effect of co2 bubbling into aqueous solutions used for electrochemical reduction of co2 for energy conversion and storage," *The Journal of Physical Chemistry C*, vol. 119, pp. 55–61, 01 2015.

[12] S. Lee, J. D. Ocon, Y.-i. Son, and J. Lee, "Alkaline co2 electrolysis toward selective and continuous hcoo–production over sno2 nanocatalysts," *The Journal of Physical Chemistry C*, vol. 119, pp. 4884–4890, 03 2015.

[13] S. Garg, M. Li, A. Z. Weber, L. Ge, L. Li, V. Rudolph, G. Wang, and T. E. Rufford, "Advances and challenges in electrochemical co2 reduction processes: an engineering and design perspective looking beyond new catalyst materials," *J. Mater. Chem. A*, vol. 8, pp. 1511–1544, 2020.

[14] M. Schwartz, R. L. Cook, V. M. Kehoe, R. C. MacDuff, J. Patel, and A. F. Sammells, "Carbon dioxide reduction to alcohols using perovskite-type electrocatalysts," *Journal of The Electrochemical Society*, vol. 140, pp. 614–618, mar 1993.

[15] R. L. Cook, R. C. MacDuff, and A. F. Sammells, "On the electrochemical reduction of carbon dioxide at in situ electrodeposited copper," *Journal of The Electrochemical Society*, vol. 135, pp. 1320–1326, jun 1988.

[16] R. L. Cook, R. C. MacDuff, and A. F. Sammells, "Efficient high rate carbon dioxide reduction to methane and ethylene at in situ electrodeposited copper electrode," *Journal of The Electrochemical Society*, vol. 134, pp. 2375–2376, sep 1987.

[17] B. Qin, Y. Li, H. Wang, G. Yang, Y. Cao, H. Yu, Q. Zhang, H. Liang, and F. Peng, "Efficient electrochemical reduction of co2 into co promoted by sulfur vacancies," *Nano Energy*, vol. 60, pp. 43–51, 2019.

[18] B. N. S. W. W. K.-H. L. S. e. a. Daiyan R, Lovell EC, "Modulating activity through defect engineering of tin oxides for electrochemical co2 reduction," *Adv Sci*, vol. 6, 2019.

[19] W. Luo, J. Zhang, M. Li, and A. Züttel, "Boosting co production in electrocatalytic co2 reduction on highly porous zn catalysts," *ACS Catalysis*, vol. 9, pp. 3783–3791, 05 2019.

[20] S. A. D. L. P.-B. T. Q.-B. R. e. a. Kibria MG, Dinh C-T, "A surface reconstruction route to high productivity and selectivity in co2 electroreduction toward c2+ hydrocarbons," *Adv Mater*, vol. 30, 2018.

[21] M. Alvarez-Guerra, A. Del Castillo, and A. Irabien, "Continuous electrochemical reduction of carbon dioxide into formate using a tin cathode: Comparison with lead cathode," *Chemical Engineering Research and Design*, vol. 92, no. 4, pp. 692–701, 2014. ECCE9 – 9th European Congress of Chemical Engineering.

[22] Y. C. Li, D. Zhou, Z. Yan, R. H. Gonçalves, D. A. Salvatore, C. P. Berlinguette, and T. E. Mallouk, "Electrolysis of co2 to syngas in bipolar membrane-based electrochemical cells," *ACS Energy Letters*, vol. 1, pp. 1149–1153, 12 2016.

[23] I. A. Merino-Garcia I, Albo J, "Productivity and selectivity of gas-phase co2 electroreduction to methane at copper nanoparticle-based electrodes," *Energy Technology*, vol. 5, 2017.

[24] R. L. Cook, R. C. MacDuff, and A. F. Sammells, "High rate gas phase CO_2 reduction to ethylene and methane using gas diffusion electrodes," *Journal of The Electrochemical Society*, vol. 137, pp. 607–608, feb 1990.

[25] J. Hereijgers, H. Ottevaere, T. Breugelmans, and W. De Malsche, "Membrane deflection in a flat membrane microcontactor: Experimental study of spacer features," *Journal of Membrane Science*, vol. 504, pp. 153–161, 2016.

[26] D. T. Whipple, E. C. Finke, and P. J. A. Kenis, "Microfluidic reactor for the electrochemical reduction of carbon dioxide: The effect of pH," *Electrochemical and Solid-State Letters*, vol. 13, no. 9, p. B109, 2010.

[27] S.-W. Kim, M. Park, H. Kim, K. J. Yoon, J.-W. Son, J.-H. Lee, B.-K. Kim, J.-H. Lee, and J. Hong, "In-situ nano-alloying pd-ni for economical control of syngas production from high-temperature thermo-electrochemical reduction of steam/co2," *Applied Catalysis B: Environmental*, vol. 200, pp. 265–273, 2017.

[28] K. Chen, X. Zhang, T. Williams, L. Bourgeois, and D. R. MacFarlane, "Electrochemical reduction of co2 on core-shell cu/au nanostructure arrays for syngas production," *Electrochimica Acta*, vol. 239, pp. 84–89, 2017.

[29] Y. Shi, Y. Luo, N. Cai, J. Qian, S. Wang, W. Li, and H. Wang, "Experimental characterization and modeling of the electrochemical reduction of co2 in solid oxide electrolysis cells," *Electrochimica Acta*, vol. 88, pp. 644–653, 2013.

[30] S. Xu, S. Li, W. Yao, D. Dong, and K. Xie, "Direct electrolysis of co2 using an oxygen-ion conducting solid oxide electrolyzer based on la0.75sr0.25cr0.5mn0.5o3 electrode," *Journal of Power Sources*, vol. 230, pp. 115–121, 2013.

[31] L. Zhang, S. Hu, X. Zhu, and W. Yang, "Electrochemical reduction of co2 in solid oxide electrolysis cells," *Journal of Energy Chemistry*, vol. 26, no. 4, pp. 593–601, 2017.

[32] "Co-electrolysis of co2 and h2o in high-temperature solid oxide electrolysis cells: Recent advance in cathodes," *Journal of Energy Chemistry*, vol. 26, no. 5, pp. 839–853, 2017. CO2 Capture Storage and Utilization.

[33] R. J. Lim, M. Xie, M. A. Sk, J.-M. Lee, A. Fisher, X. Wang, and K. H. Lim, "A review on the electrochemical reduction of co2 in fuel cells, metal electrodes and molecular catalysts," *Catalysis Today*, vol. 233, pp. 169–180, 2014. Catalytic Materials And Catalysis For Low Carbon Technology.

[34] S. D. Ebbesen, S. H. Jensen, A. Hauch, and M. B. Mogensen, "High temperature electrolysis in alkaline cells, solid proton conducting cells, and solid oxide cells," *Chemical Reviews*, vol. 114, pp. 10697–10734, 11 2014.

[35] B. C. Marepally, C. Ampelli, C. Genovese, F. Tavella, E. A. Quadrelli, S. Perathoner, and G. Centi, "Electrocatalytic reduction of co2 over dendritic-type cu- and fe-based electrodes prepared by electrodeposition," *Journal of CO2 Utilization*, vol. 35, pp. 194–204, 2020.

[36] P. Jeanty, C. Scherer, E. Magori, K. Wiesner-Fleischer, O. Hinrichsen, and M. Fleischer, "Upscaling and continuous operation of electrochemical co2 to co conversion in aqueous solutions on silver gas diffusion electrodes," *Journal of CO2 Utilization*, vol. 24, pp. 454–462, 2018.

[37] B. C. Marepally, C. Ampelli, C. Genovese, F. Tavella, L. Veyre, E. A. Quadrelli, S. Perathoner, and G. Centi, "Role of small cu nanoparticles in the behaviour of nanocarbon-based electrodes for the electrocatalytic reduction of co2," *Journal of CO2 Utilization*, vol. 21, pp. 534–542, 2017.

[38] M. Ramdin, A. R. T. Morrison, M. de Groen, R. van Haperen, R. de Kler, L. J. P. van den Broeke, J. P. M. Trusler, W. de Jong, and T. J. H. Vlugt, "High pressure electrochemical reduction of co2 to formic acid/formate: A comparison between bipolar membranes and cation exchange membranes," *Industrial & Engineering Chemistry Research*, vol. 58, pp. 1834–1847, 02 2019.

[39] Z. Liu, R. I. Masel, Q. Chen, R. Kutz, H. Yang, K. Lewinski, M. Kaplun, S. Luopa, and D. R. Lutz, "Electrochemical generation of syngas from water and carbon dioxide at industrially important rates," *Journal of CO2 Utilization*, vol. 15, pp. 50–56, 2016. Special Issue on the XIII International Conference on Carbon Dioxide Utilization (ICCDU-2015).

[40] J. J. Kaczur, H. Yang, Z. Liu, S. D. Sajjad, and R. I. Masel, "Carbon dioxide and water electrolysis using new alkaline stable anion membranes," *Frontiers in Chemistry*, vol. 6, 2018.

[41] B. Endrődi, E. Kecsenovity, A. Samu, F. Darvas, R. V. Jones, V. Török, A. Danyi, and C. Janáky, "Multilayer electrolyzer stack converts carbon dioxide to gas products at high pressure with high efficiency," *ACS Energy Letters*, vol. 4, pp. 1770–1777, 07 2019.

[42] G. O. Larrazábal, P. Strøm-Hansen, J. P. Heli, K. Zeiter, K. T. Therkildsen, I. Chorkendorff, and B. Seger, "Analysis of mass flows and membrane crossover in co2 reduction at high current densities in an mea-type electrolyzer," *ACS Applied Materials & Interfaces*, vol. 11, pp. 41281–41288, 11 2019.

[43] D. A. Vermaas and W. A. Smith, "Synergistic electrochemical co2 reduction and water oxidation with a bipolar membrane," *ACS Energy Letters*, vol. 1, pp. 1143–1148, 12 2016.

[44] X. Zhou, R. Liu, K. Sun, Y. Chen, E. Verlage, S. A. Francis, N. S. Lewis, and C. Xiang, "Solar-driven reduction of 1 atm of co2 to formate at 10% energy-conversion efficiency by use of a tio2-protected iii–v tandem photoanode in conjunction with a bipolar membrane and a pd/c cathode," *ACS Energy Letters*, vol. 1, pp. 764–770, 10 2016.

[45] T. N. Nguyen and C.-T. Dinh, "Gas diffusion electrode design for electrochemical carbon dioxide reduction," *Chem. Soc. Rev.*, vol. 49, pp. 7488–7504, 2020.

[46] Y. Hori, *Electrochemical CO2 Reduction on Metal Electrodes*, pp. 89–189. New York, NY: Springer New York, 2008.

[47] A. Bagger, W. Ju, A. S. Varela, P. Strasser, and J. Rossmeisl, "Electrochemical co2 reduction: Classifying cu facets," *ACS Catalysis*, vol. 9, pp. 7894–7899, 09 2019.

[48] K. J. P. Schouten, Z. Qin, E. Pérez Gallent, and M. T. M. Koper, "Two pathways for the formation of ethylene in co reduction on single-crystal copper electrodes," *Journal of the American Chemical Society*, vol. 134, pp. 9864–9867, 06 2012.

[49] T. Zhang, J. C. Bui, Z. Li, A. T. Bell, A. Z. Weber, and J. Wu, "Highly selective and productive reduction of carbon dioxide to multicarbon products via in situ co management using segmented tandem electrodes," *Nature Catalysis*, vol. 5, no. 3, pp. 202–211, 2022.

[50] E. Bormashenko, Y. Bormashenko, and M. Frenkel, "Formation of hierarchical porous films with breath-figures self-assembly performed on oil-lubricated substrates," *Materials*, vol. 12, no. 18, 2019.

[51] N. Elgrishi, K. J. Rountree, B. D. McCarthy, E. S. Rountree, T. T. Eisenhart, and J. L. Dempsey, "A practical beginner's guide to cyclic voltammetry," *Journal of Chemical Education*, vol. 95, no. 2, pp. 197–206, 2018.

[52] A. Sacco, "Electrochemical impedance spectroscopy: Fundamentals and application in dye-sensitized solar cells," *Renewable and Sustainable Energy Reviews*, vol. 79, pp. 814–829, 2017.

[53] J. Zeng, T. Rino, K. Bejtka, M. Castellino, A. Sacco, M. A. Farkhondehfal, A. Chiodoni, F. Drago, and C. F. Pirri, "Coupled copper–zinc catalysts for electrochemical reduction of carbon dioxide," *ChemSusChem*, vol. 13, no. 16, pp. 4128–4139, 2020.